BRILLOUIN SCATTERING INDUCED TRANSPARENCY AND GENERATION OF SLOW AND FAST LIGHT

BY

JUNHWAN KIM

THESIS

Submitted in partial fulfillment of the requirements
for the degree of Master of Science in Mechanical Engineering
in the Graduate College of the
University of Illinois at Urbana-Champaign, 2014

Urbana, Illinois

Adviser:

Assistant Professor Gaurav Bahl

ABSTRACT

Electromagnetically induced transparency (EIT) is generation of a narrow window in which electromagnetic field absorption is inhibited. Experimentally, a probe tuned to a certain absorption wavelength is allowed to transmit through a gaseous vapor only in the presence of a second control laser. In other words, a probe is forbidden to cause an excitation from one energy level to another through coherent coupling with a third, intermediate energy level that creates an interference pathway. In this study, Brillouin scattering analogue of EIT is demonstrated using the two optical modes that are coupled through a phase matched acoustic mode. The coherent coupling of two energy levels is emulated by the acousto-optic interaction of Brillouin scattering. The probe phase response is analyzed to estimate BSIT's effect on the velocity of light pulse. As BSIT modifies the dispersion of light, it is understood as either slowing or advancing light propagation depending on the sign of the slope of the probe phase response. Lastly, the non-reciprocity of Brillouin scattering is theoretically considered. The non-reciprocity, or a break in time reversal symmetry, is a unique property of Brillouin scattering process due to the traveling surface acoustic wave which is used for phase matching the optical modes. Therefore, BSIT can be used for applications such as optical isolation while no other transparency systems can.

ACKNOWLEDGMENTS

I would like to thank

My advisor Dr. Gaurav Bahl for encouragement and guidance in preparation of this thesis work.

My colleagues Kewen Han, Seunghwi Kim, and Shiyi Chen for thought provoking discussions.

My parents for supporting me financially and spiritually for I will not be here without them.

My wife JeeYeun for her continued support, love and understanding through difficult times, and her parents for their kindness and patience.

Lastly, my son Ian, the newest addition to my family, for bringing joy and happiness.

TABLE OF CONTENTS

CHAPTER 1

INTRODUCTION

To understand Brillouin scattering induced transparency (BSIT), necessary background on Brillouin scattering and electromagnetically induced transparency (EIT) are provided in this chapter.

1.1 Motivation

The initial motivation for our project on BSIT was to explore a mechanism (i.e. Brillouin scattering) with which the transparency phenomena have been considered infeasible. Induced transparency using Brillouin scattering is difficult to achieve because of the long coherence phonon lifetime required for the transparency. However, we show that a high coherence phonon mode of forward Brillouin scattering can enable the transparency phenomena.

After our first experiment, it was realized that this BSIT system is also suitable for slow and fast light generation. Using a high quality factor microsphere resonator, our BSIT system was able to achieve the comparable time delay and bandwidth with only a fraction of laser power and device size (Table 3.1).

Lastly, the non-reciprocity of Brillouin scattering can be used for creating a non-magnetic optical isolator. Optical isolators are essential components in many optical systems for protecting laser sources and components vulnerable to backscattered or reflected light fields. Up to date, all optical isolators were based on the principles of Faraday rotation which describes a dielectric material's phenomenon that rotates the light polarization non-reciprocally based on an applied magnetic field. Therefore, we propose that our new optical isolator design based on BSIT may be useful in applications where the use of magnetic fields is difficult or prohibited.

1.2 Brillouin Scattering

In general, light scattering occurs due to some fluctuation in the propagation medium. For instance, Rayleigh scattering and Mie scattering are caused from the fluctuation in density, and Raman scattering is caused from the molecular vibration. Brillouin scattering is caused from the interaction of light and acoustic waves (acousto-optic interaction).

1.2.1 Spontaneous and Stimulated Brillouin Scattering

Spontaneous Brillouin scattering process starts when light interacts with the refractive index perturbations that are caused by the presence of an acoustic wave within a medium [1]. The spatio-temporal beat of the incident and scattered light fields then create a periodic variation in refractive index through electrostriction pressure, which is a property of a dielectric material to become more dense under electromagnetic field. In the case that light is scattered to lower frequencies (i.e. Stokes scattering), the electrostriction pressure imparts energy to the sound wave. On the other hand, for anti-Stokes scattering, energy is removed from the sound wave, leading to cooling and linewidth broadening [2]. By definition, Brillouin scattering is considered spontaneous when the material property can be assumed to be unchanged from the incident light. However, when sufficient input laser power is provided, the Stokes scattering process can overcome all intrinsic losses, resulting in the formation of a Brillouin laser through Stimulated Brillouin Scattering (SBS) [1, 3].

1.2.2 Phase Matching

As shown in Fig. 1.2, for both forward scattering and back-scattering, very specific energy conservation (Eq. 1.2) and momentum conservation (Eq. 1.1) requirements must be satisfied for Brillouin scattering processes to take place (i.e. phase matching).

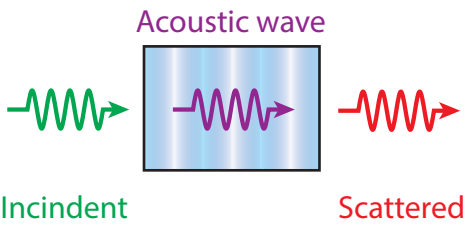

Figure 1.1: Brillouin scattering occurs due to the acoustic wave that creates a refractive index perturbations within the medium. For spontaneous Brillouin scattering, light field creates only a small change in material property. However, when the incident light field exceeds the threshold power, stimulated Brillouin scattering occurs and the acoustic wave is reinforced. In other words, Brillouin gain overcomes the optical loss from the material. The direction of scattered field propagation is not necessarily forwards as illustrated, but can be in any direction.

$$\vec{k}_2 - \vec{k}_1 = \vec{q}_B \tag{1.1}$$

$$\omega_2 - \omega_1 = \Omega_B \tag{1.2}$$

In a back-scattering SBS system, the optical fields propagate in opposite directions. Since the frequencies, ω_1 and ω_2, are nearly identical, the optical momentum vectors, $\vec{k}_1$ and $\vec{k}_2$, are also nearly identical, but have opposite signs (propagating in the opposite direction). Thus, acoustic momentum vector, $\vec{q}_B$, is about double the length of the optical momentum vector to satisfy Eq. 1.1 and 1.2 as shown in Fig. 1.2b and 1.3b. This implies the generation of acoustic waves in the tens of GHz frequency regime, depending on the laser frequency, ω, refractive index, n, and speed of sound in the material, v (Eq. 1.3) [1]. In case of silicon dioxide excited with a 193 THz (1550 nm) laser, the Brillouin frequency is 11 GHz ($v = 5700$ m/s, $n = 1.5$).

$$\Omega_B = \frac{2v}{c/n}\omega \tag{1.3}$$

In a forward-SBS system, the momentum vectors of the incident and scattered light are nearly identical with the same sign (propagating in the same direction) as shown in Fig. 1.2a. Hence, the acoustic momentum vector is very small and the frequency is typically in a sub-GHz (Eq. 1.4).

$$\vec{q}_B = \frac{\Omega_B}{\vec{v}} \tag{1.4}$$

At such low frequency, the phonon lifetimes are significantly longer than that of the acoustic mode from back-scattering.

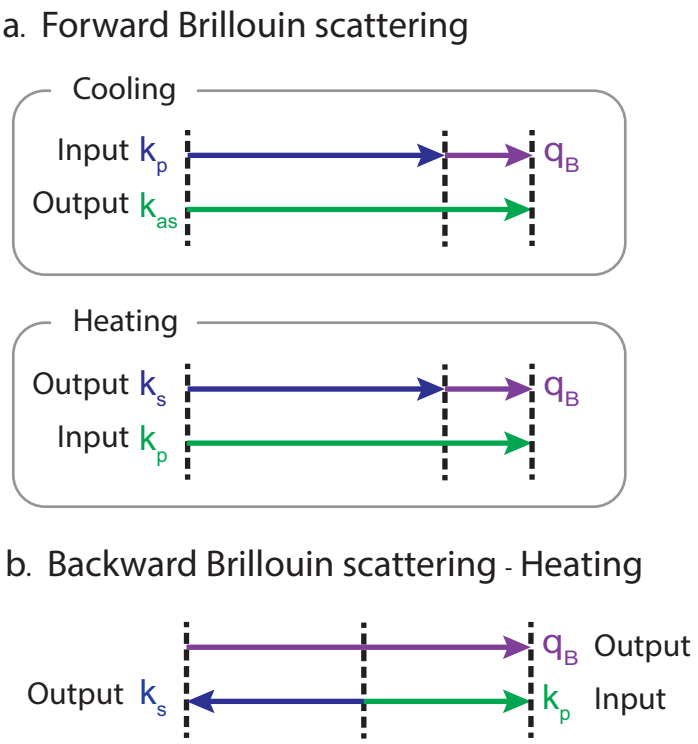

Figure 1.2: **a.** Phase matching for forward Brillouin scattering. The co-propagating optical fields are phase matched by a low frequency acoustic mode, q_B. (Top) Input laser field k_p can scatter to a anti-Stokes field k_{as} and annihilate acoustic field q_B, i.e. cooling. (Bottom) When the laser is parked at the high frequency mode, the input laser field k_p can scatter to a Stokes field k_s and reinforce acoustic field q_B, i.e. heating. **b.** Phase matching for backward Brillouin scattering. The counter propagating optical fields, k_p and k_s, are phase matched by a high frequency acoustic mode, q_B. The input laser field k_p scatters in the backward direction to a Stokes field k_s and high frequency acoustic field q_B is launched.

1.3 Electromagnetically Induced Transparency

Electromagnetically induced transparency (EIT) is described as an inhibited absorption of electromagnetic field within an atomic absorption line. Typi-

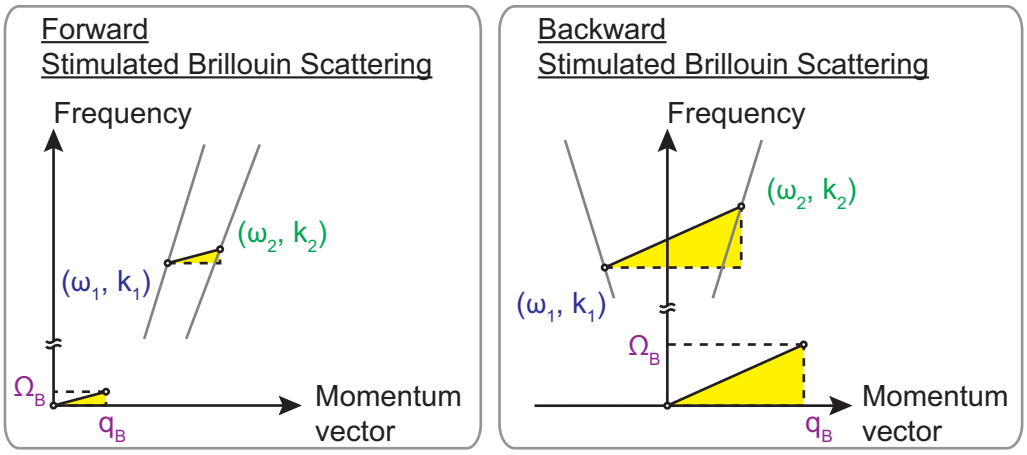

Figure 1.3: Dispersion diagrams. When the control laser is parked at high frequency optical mode, (ω_2, k_2), Stokes scattered light is generated at low frequency optical mode, (ω_1, k_1). For Stokes scattering, the frequencies and wave vectors of the two optical modes and an intermediate acoustic mode must satisfy the condition, $k_2 - k_1 = q_B$ and $\omega_2 - \omega_1 = \Omega_B$. (left) Forward-SBS system. (right) Backward-SBS system.

cally, an electromagnetic field tuned to an absorption line will be absorbed to the material and excite an electron to the higher state. In EIT, a strong electromagnetic field (control laser) is set at a frequency matching the transition from an intermediate state to the excited state (|2>-|3> transition from Fig. 1.5a). In effect, the control laser enables an indirect transition pathway for a weak electromagnetic field (probe laser). Then, the destructive interference of the direct and indirect transition pathways takes place and reveals itself as an induced transparency (Fig. 1.4b). Here, it is important to note that the two energy levels must be coherently coupled with sufficient coupling rate (Rabi frequency) for the noticeable effect in the absorption line.

Experimentally, EIT was first observed by Boller et. al. in an absorption line of strontium [4]. In the energy level diagram of strontium (Fig. 1.5a), a lambda type system with energy levels and transition pathways suitable for interference is shown. In the presence of the strong control laser tuned to |2>-|3> transition, the direct probe transition |1>-|3> and the indirect probe transition |1>-|3>-|2>-|3> have opposite signs of probability amplitude and thus destructively interfere. An illustration of probe transmission signal is shown in Fig. 1.5b.

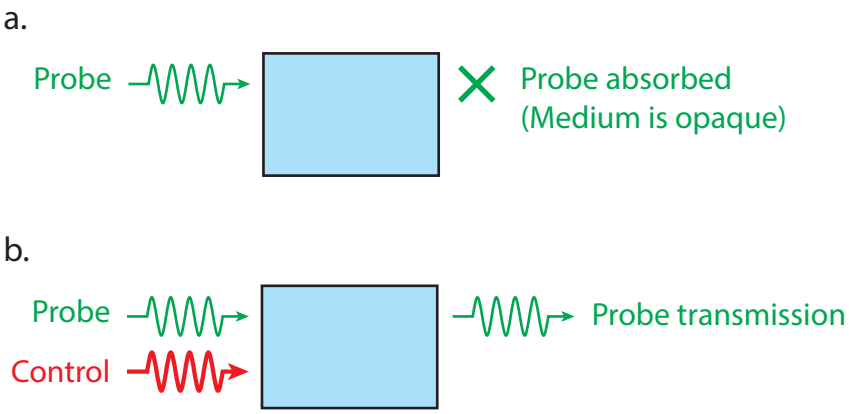

Figure 1.4: **a.** Probe signal is absorbed without the control laser. In other words, the medium is opaque at the probe frequency. **b.** Probe at the absorption frequency is allowed to transmit through the medium when the control laser creates two transition pathways for the probe.

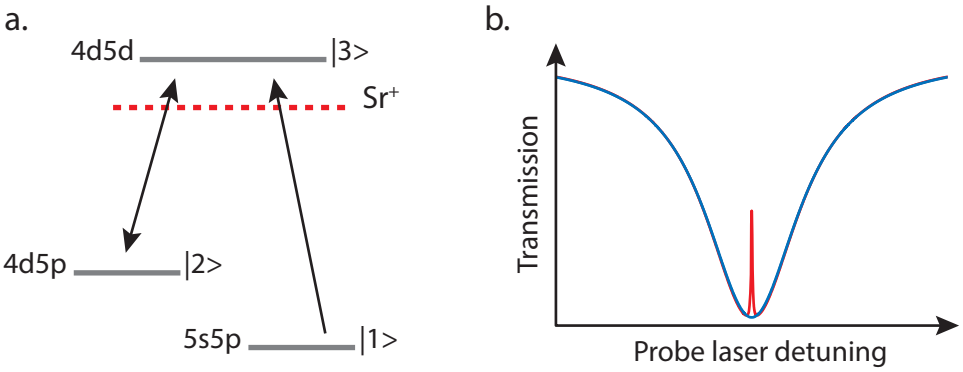

Figure 1.5: **a.** Lambda type energy level diagram of strontium. **b.** (Blue) Probe transmission showing an absorption line without EIT. (Red) In the presence of the control laser, induced transparency is observed within the absorption line.

1.4 Induced Transparency in Other Systems

Since the first demonstration of induced transparency in 1991 [4], there have been several successful attempts to emulate analogous phenomenon in other systems. Zhang et. al. theoretically suggested induced transparency in plasmonic system [5] and Liu et. al. carried out the experiment [6]. In this plasmonic system, two non-radiative mode coupled with a superradiant mode form an EIT-like resonance with a narrow region of destructive interference. Smith et. al. demonstrated induced transparency using two coupled resonators [7]. In the coupled resonator system, the light traveling

within only one resonator and the light that traveled through the second resonator are allowed to destructively interfere as the phase shift is introduced from the light coupling to another resonator. Weis et. al. demonstrated optomechanically induced transparency using an optical microcavity [8] and Safavi-Naeini et. al. using optomechanical crystal nanocavity [9]. In both optomechanical analogue of EIT, the two optical fields are coupled through an acoustic excitation and annihilation. This acoustic excitation and annihilation process creates a second transition pathway similar to the indirect transition pathway of EIT.

Brillouin scattering has been considered infeasible for induced transparency because the coherence of the phonon mode in backward-SBS is very low. However, Bahl et. al. demonstrated Brillouin cooling in which the high coherence phonon mode of forward anti-Stokes scattering was explored [2]. In this work, induced transparency is demonstrated using the high coherence phonon mode of the forward anti-Stokes scattering identical to Brillouin cooling demonstration.

CHAPTER 2

BRILLOUIN SCATTERING INDUCED TRANSPARENCY

With a necessary background on Brillouin scattering and EIT, the theoretical description and experimental result of Brillouin scattering induced transparency (BSIT) is presented in this chapter. Just like EIT, BSIT is observed as a small window of inhibited absorption within an optical resonance. The key difference is that the phase matched set of optical and acoustic modes of a resonator is used instead of an atomic excitation.

2.1 Energy Level Analogy of Brillouin Scattering

A 3-level lambda system analogy to EIT (Fig. 1.5a) can be made in the case of BSIT as shown in Fig. 2.1. Here, the optical mode (ω_1, k_1) is represented as an absorption transition |1>-|e>. For our BSIT experiment (Fig. 2.1a), the control laser is parked at the low frequency optical mode |2>-|e> while the probe laser is parked at the high frequency optical mode |1>-|e>. The separation of the two optical modes in a frequency space is defined by the acoustic frequency of Brillouin scattering, $\hbar\Omega_B$. Although light cannot directly scatter from |1> to |2> or vice versa, the two levels are coherently coupled via Brillouin scattering. With the coupling established, the probe transition through the direct path |1>-|e> interferes with the indirect transition path |1>-|e>-|2>-|e>. This interference results in the inhibited absorption.

Similarly, Stokes scattering is represented using energy level diagram in Fig. 2.1b. In this case, the constructive interference causes increased absorption into the optical mode as will be shown in Ch. 2.4.3.

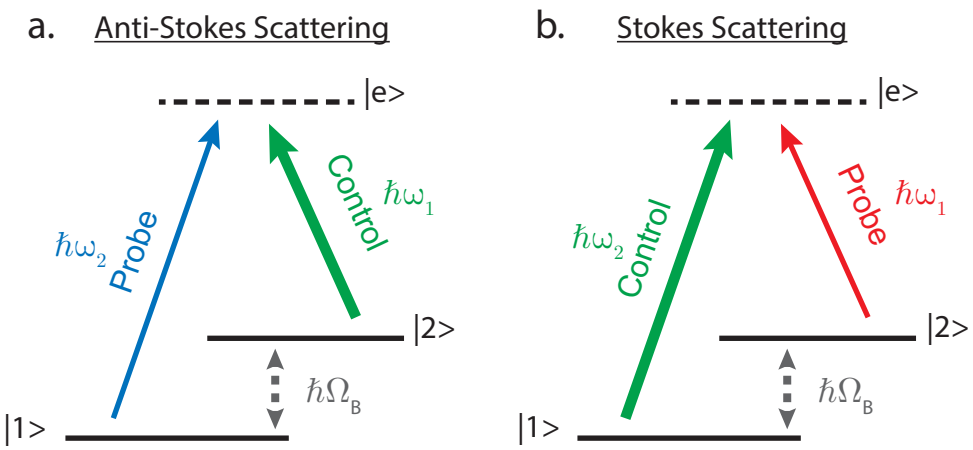

Figure 2.1: **Energy level analogy for Brillouin scattering systema.** Energy level with transition pathways for anti-Stokes scattering. Control laser is parked at the lower frequency transition |2>-|e> where |e> is a virtual level. **b.** Energy level with transition pathways for Stokes scattering. Control laser is now parked at higher frequency transition |1>-|e>.

2.2 Requirement for Observation of Brillouin Scattering Induced Transparency

The generation of BSIT requires a 3-mode system composed of two optical modes and one long-lived acoustic mode forming an aforementioned energy level analogue of EIT. Here, the long-lived acoustic mode allows sufficient coupling between the two optical modes before decoherence. Phase-matching of these modes in both frequency space and momentum space is essential as illustrated in Fig. 1.3. Notably, the momentum requirement is not needed for other transparency mechanisms [4, 8, 9, 10, 11]. As mentioned previously, in BSIT, the energies and momenta of these three modes must be matched to satisfy $\omega_2 - \omega_1 = \Omega_B$ and $k_2 - k_1 = q_B$ simultaneously. Here, (ω_1, k_1) are the energy and momentum of the lower energy optical mode, (ω_2, k_2) represent the higher energy optical mode, and (Ω_B, q_B) represent the acoustic mode. The coupling between the three modes is mediated by electrostrictive Brillouin scattering. Previous work has shown that such instances of both forward- and backward-SBS phase matching can occur naturally within a microresonator [2, 12, 13, 14].

Consider the situation where a strong laser pumps the lower energy optical

mode (ω_1, k_1) while a weaker tunable probe measures the higher energy optical mode (ω_2, k_2) of the coupled system (Fig. 2.1a). When the anti-Stokes probe signal is tuned to a resonator mode, it couples strongly to the resonator and generates a well understood opacity in the waveguide (Fig. 2.2,bottom) [15]. Further, in the presence of Brillouin phase match of the strong control laser and the anti-Stokes probe with a long lived phonon mode in the same medium, the probe is expected to undergo very strong resonant absorption into the control signal (Fig. 2.2,top) [16]. Intuitively, these two cascaded stages of absorption should lead to near-complete removal of the probe light from the system. As shown in this BSIT system, the intuition breaks down, and instead of strong absorption of the anti-Stokes probe, an interference is generated between the Stokes-directed absorption and anti-Stokes-directed scattering pathways. This results in a previously unforeseen transparency at the probe frequency $\omega_p = \omega_c + \Omega_B$ and the probe no longer couples into the resonator optical mode (Fig. 2.2).

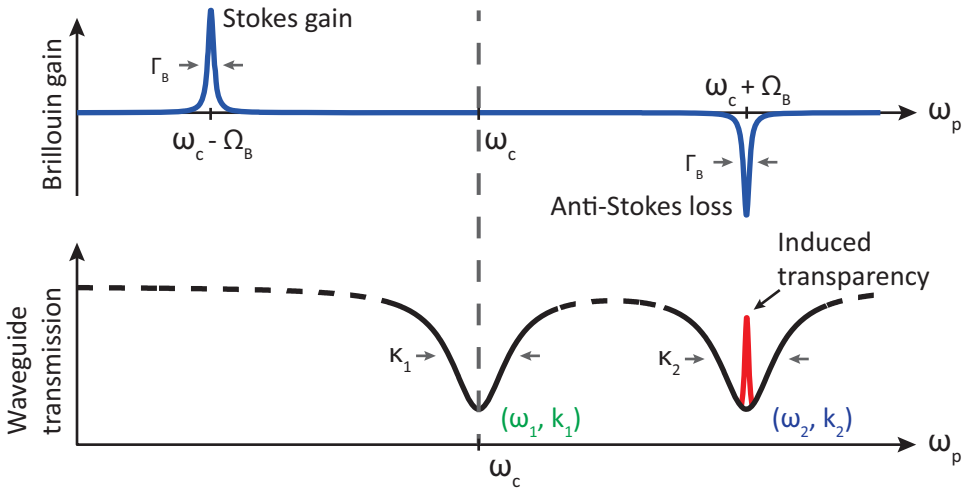

Figure 2.2: The control laser pumps the lower frequency optical mode to allow anti-Stokes scattering while the resonator suppresses Stokes scattering [2]. (Bottom) A probe laser scans through the optical resonances, visible as a drop in waveguide transmission [15]. (Top) From traditional SBS theory [1] anti-Stokes absorption is predicted for a probe signal at $\omega_p = \omega_c + \Omega_B$, which intuitively should increase the probe loss. However, when (Ω_B, q_B) represent a long lived phonon mode, a transparency is observed due to interference between Stokes and anti-Stokes scattering pathways.

2.3 Methodology

2.3.1 Fabrication of Tapered Coupler and Resonator

A tapered coupler is fabricated to provide a means to couple light in and out of the resonator. First demonstrated by J. C. Knight, the tapered coupler is a technique based on the principles of evanescent light coupling [17]. Compared to other light coupling techniques such as freespace coupling [18] or prism coupling [19], tapered coupler is more easily fabricated and maneuvered while still allowing high coupling efficiency. The tapered coupler is fabricated by applying high heat to the fiber using hydrogen flame and simultaneously applying tension by pulling both ends of the fiber (Fig. 2.3). Using this technique, a single mode fiber with outside diameter of 125 μm (Corning SMF-28e+ fiber [20]) is scaled down to sub-μm in diameter. When the diameter of the fiber is smaller than the wavelength of the laser, the light can effectively couple to the resonator in proximity.

The microsphere resonator device is also fabricated using the fiber material. The use of the same material allows efficient light coupling without a necessity to control how much light couples from tapered coupler to the resonator and vice versa. The resonator can be made from nearly any dielectric materials given the optical transmission spectrum with low absorption at the laser wavelength in use. Use of different resonator material is discussed in Ch. 5.1. For the fabrication, the tip of the broken fiber is melted to naturally form a sphere from surface tension. The heat is supplied by an electric arc discharge from a fusion splicer (Ericsson FSU 975 [21]). Also, the use of broken tapered fiber allows the fabrication of even smaller microsphere with the sub-100 μm in diameter while still maintaining high mechanical and optical quality factor.

2.3.2 Experimental Procedure

Fig. 2.4 shows the experimental setup used in this work. An ultra-high-Q silica microsphere resonator is evanescently coupled to a tapered silica fiber waveguide (Fig. 2.5), that provides coupling mechanism to the intracavity control and probe light fields. A tunable diode laser with a center wavelength of 1550 nm provides the control field to the pump mode, while the probe signal is generated using an electro-optic modulator (EOM). While the EOM

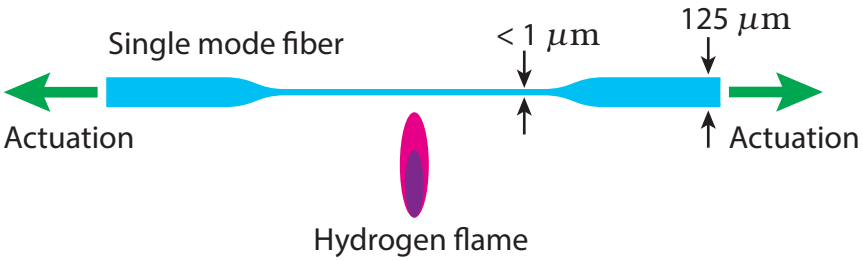

Figure 2.3: Tapered coupler fabrication. Single mode fiber is pulled in opposite direction while heat from hydrogen flame is applied. The resonator is coupled by placing the tapered coupler in proximity (Fig. 2.5b).

creates two probe sidebands relative to the control laser, only one sideband is matched to the anti-Stokes optical mode of the device. The other (Stokes) sideband does not couple to the resonator and passes through the system unhindered at constant amplitude. The probe sideband spacing is determined by a modulation signal input to the EOM that is generated by a network analyzer. The transmitted optical signal at the output of the waveguide is received by a highspeed photodetector (Newport Model 1601 [22]), which results in an electronic output beat note between the control and probe optical signals. This electronic output is analyzed by an electrical spectrum analyzer (Tektronix RSA6120A [23]) as well as the network analyzer (Agilent 4395A [24]) for probe transfer function analysis. When the higher energy optical mode is pumped above threshold (in the absence of a probe), the electronic beat note between the pump and scattered light generated on a photodetector can be used to distinguish the Brillouin scattering [2, 12] from radiation pressure induced optomechanical oscillation [25].

2.4 Experimental Result

2.4.1 Verification of Brillouin Phase Matching

First task is to find a set of optical modes and an acoustic mode that fulfills the phase matching (Eq. 1.1 and 1.2) and allows the Brillouin scattering. Following the procedure from Ch. 2.3.2, the Brillouin phase matching is verified by the lack of harmonics from the beat note between the pump and scattered light. The beat notes generated from the two sets of optical fields used for

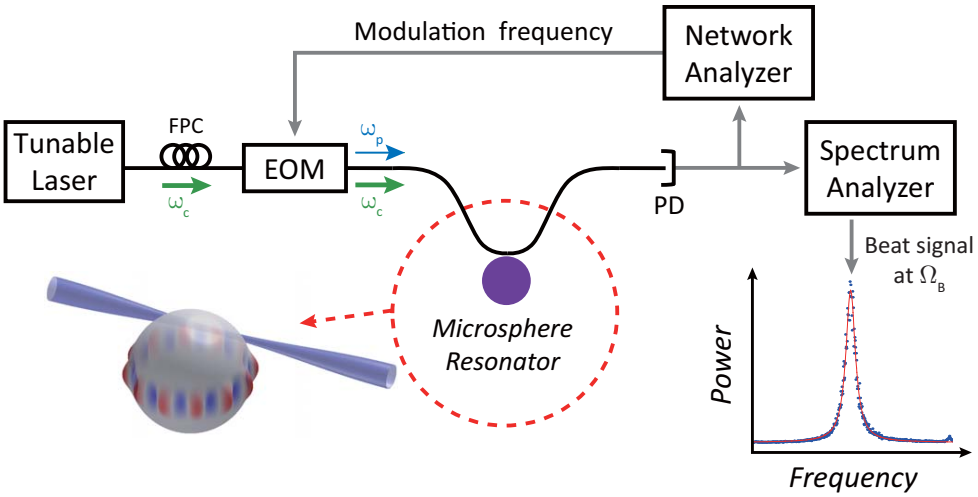

Figure 2.4: Experimental setup. Fiber coupled tunable diode laser sends the control laser signal through a tapered waveguide. Network analyzer provides probe frequency to the electro-optic modulator which creates a probe signal from the control laser. Photodetector (PD) monitors the signal transmission at the waveguide output and the electronic signal is analyzed using both network analyzer and electrical spectrum analyzer. FPC is fiber polarization controller.

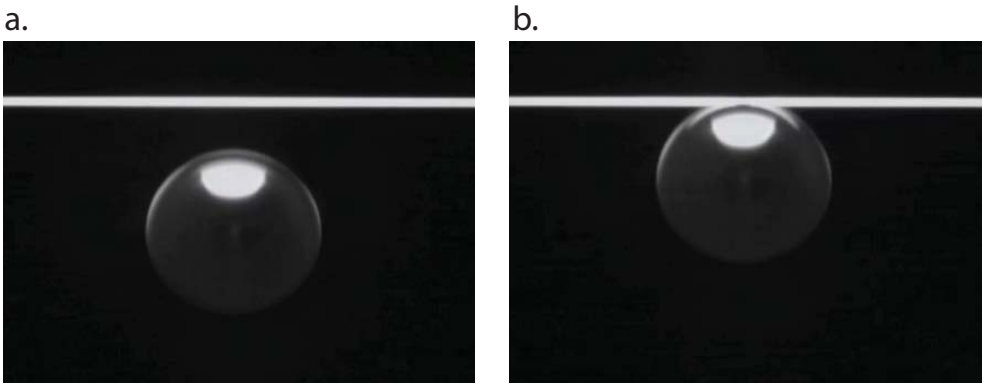

Figure 2.5: **Microscope images of resonator a.** Resonator is uncoupled from tapered coupler. **b.** Resonator is coupled to tapered coupler. The distance between the resonator and tapered coupler can range between in-contact to tens of nm.

induced transparency and absorption experiments are shown in Fig. 2.6.

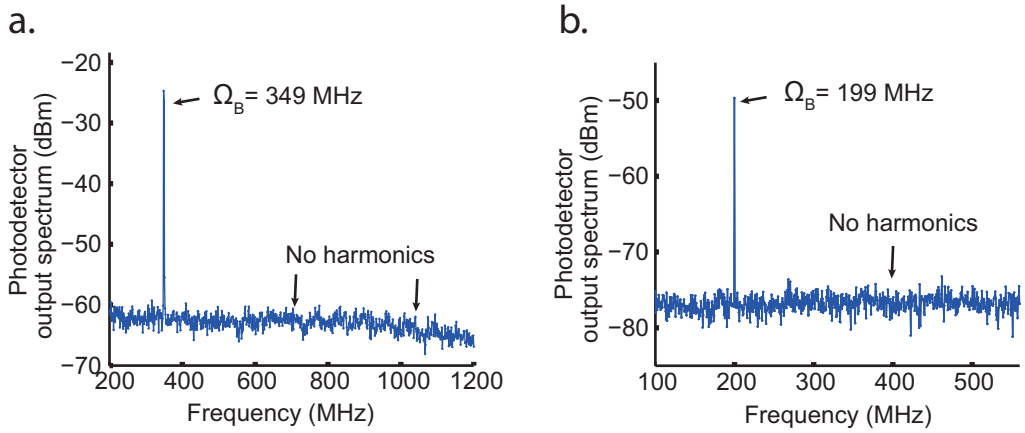

Figure 2.6: **Verification of Brillouin phase matching through Brillouin lasing. a.** When the (ω_2, k_2) mode is pumped with a strong laser source, a Stokes SBS laser is generated [12]. When the Stokes scattered and pump light are interfered on a photodetector, a beat note corresponding to their frequency difference, Ω_B, is measured. The lack of harmonics of Ω_B indicates that this is not a radiation pressure induced optomechanical oscillation. This is from induced transparency data. **b.** Brillouin lasing for induced absorption experiment (Ch. 2.4.3).

2.4.2 Induced Transparency

When the optical and acoustic modes are identified, the induced transparency experiment is carried out as described in Ch. 2.3.2. First, the control laser is parked at the lower optical resonance and a probe signal on the higher resonance. Then, it leads to destructive interference for a probe signal and generates a transparency window (Fig. 2.7a). The measured amplitude response of the probe laser in Fig. 2.7a shows the relatively broad 4.4 MHz wide anti-Stokes optical mode with optical quality factor of 4.4×10^7. A very sharp transparency feature at 349.3 MHz offset from the control laser is observed in both amplitude and phase responses of the probe (Fig. 2.7). This 349.3 MHz frequency corresponds to a whispering-gallery acoustic wave mode [12] of the resonator with azimuthal mode number of 48 and phonon lifetime of 59.2 μs.

2.4.3 Induced Absorption

If the control optical signal is tuned to the higher energy optical resonance, it creates a region of greater opacity for a probe on the lower energy optical

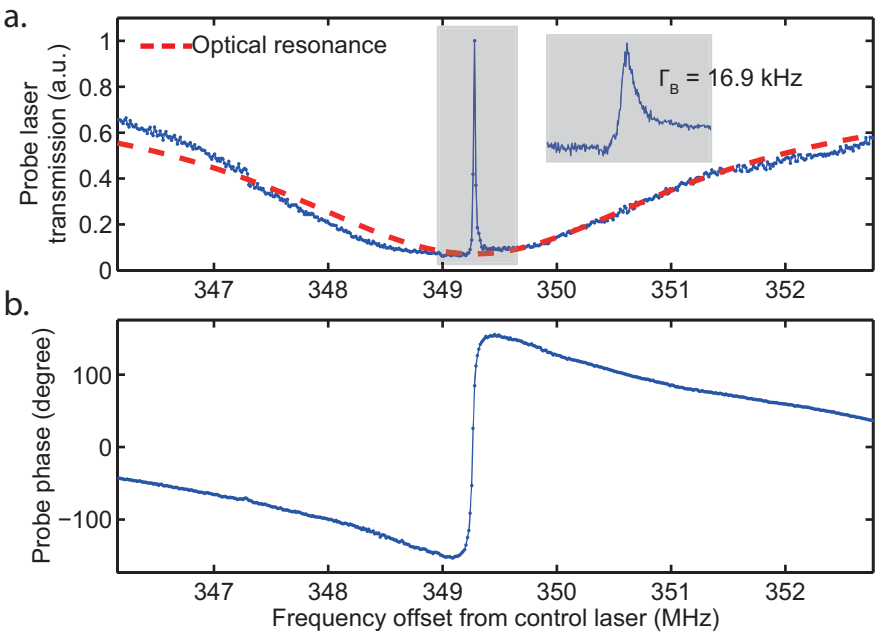

Figure 2.7: **Observation of BSIT a.** Transparency is observed for a probe on (ω_2, k_2) when a strong pump is placed at (ω_1, k_1). (Solid) Probe laser amplitude response. (Red-dashed) Curve fit to the (ω_2, k_2) optical mode. **b.** Probe phase response with distorted dispersion within the transparency.

mode (Fig. 2.8a). Due to thermal effects on the optical resonance frequencies, it was technically more convenient to demonstrate opacity with a different forward-SBS triplet on the same resonator where Ω_B= 199.8 MHz (phonon lifetime of 56.2 μs). The amplitude response of the probe laser in Fig. 2.8a shows the 0.4 MHz wide Stokes optical mode with optical quality factor of 4.9×10^8. An opacity with a 17.8 kHz linewidth is induced at 199.8 MHz offset from the pump.

2.5 Theoretical Derivation

In addition to the intuitive explanation, the induced transparency and absorption equations are rigorously derived here.

2.5.1 Induced Transparency

For the analytical description of Brillouin scattering induced transparency (BSIT), the mathematical formalism established by Agarwal and Jha is

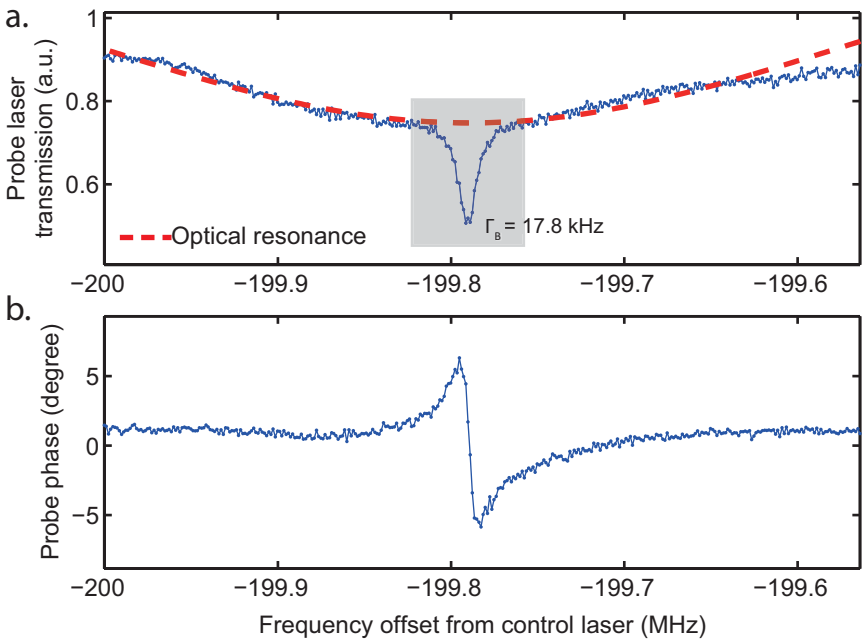

Figure 2.8: **Observation of induced absorption. a.** In the configuration shown in Fig. 2.1b, the probe experiences an opacity at Ω_B offset from the control laser. (Solid) Amplitude response of the probe laser. (Red-dashed) Curve fit to the (ω_1, k_1) optical mode. **e.** Probe phase response with distortion within the transparency. The observed phase data shows a change in slope that is opposite from that of the induced transparency phase data.

adopted [26]. The intracavity fields representing the pump/control laser, anti-Stokes shifted probe, and acoustic displacement can be described using the following three coupled rate equations.

$$\begin{aligned} \dot{a_1} &= -\kappa_1 a_1 - i\Delta_1 a_1 - i\beta^* u^* a_2 e^{-i\delta t} \\ \dot{a_2} &= -\kappa_2 a_2 - i\Delta_2 a_2 - i\beta u a_1 e^{i\delta t} \\ \dot{u} &= -\Gamma_B u - i\Delta_B u - i\beta^* a_1^* a_2 e^{-i\delta t} \end{aligned} \tag{2.1}$$

$$\begin{aligned} \delta &= \omega_2 - \omega_1 - \Omega_B \\ \Delta_1 &= \omega_1 - \omega_c \\ \Delta_2 &= \omega_2 - \omega_p \\ \Delta_B &= \Omega_B - (\omega_p - \omega_c) \end{aligned} \tag{2.2}$$

where a_1, a_2, and u are the slowly varying phasor amplitudes of intracavity control field, scattered light field and mechanical displacement respectively,

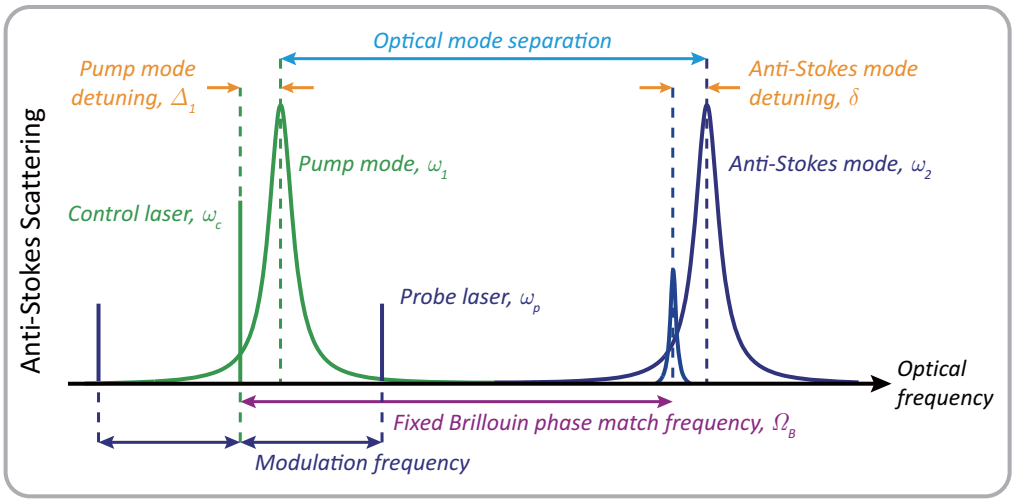

Figure 2.9: Optical frequency relationship of the coupled triplet system for transparency experiment using anti-Stokes scattering. The pump mode is at lower frequency than the anti-Stokes mode. When the modulation frequency sweeps over the fixed Brillouin phase match frequency, Ω_B, the transparency is observed in the probe response.

κ_1 and κ_2 are optical loss rates of pump mode and anti-Stokes mode respectively, Γ_B is acoustic loss rate, and β is the coupling coefficient accounting for modal overlap and Brillouin gain in the material. The frequencies ω_1, ω_2, and Ω_B represent the pump optical resonance, anti-Stokes optical resonance, Brillouin acoustic resonance, while ω_c, and ω_p represent the control laser field and probe laser field respectively. δ, Δ_1, Δ_2, and Δ_B are the pump mode to anti-Stokes mode detuning from the acoustic mode, pump mode detuning from the control laser, anti-Stokes mode detuning from the probe laser, and the modulation frequency detuning from the acoustic mode respectively.

Details on the evaluation of detuning parameters and the coupling parameter β are provided in [26]. For phase matching, the frequency relationship $\omega_2 = \omega_1 + \Omega_B$ must be satisfied. Momentum matching is implicit in the complex phasors that represent the fields.

For the induced transparency experiment, the system at steady state is analyzed, thus setting all derivatives to zero. Additional intracavity control field f_c and probe field f_p terms are added on the right-hand-side as shown in eqns. 2.3. For further simplification, the optical loss rates κ_1 and κ_2 are assumed nearly identical (new symbol κ). Finally, the non-depleted pump field approximation eliminates the coupling term from the first equation.

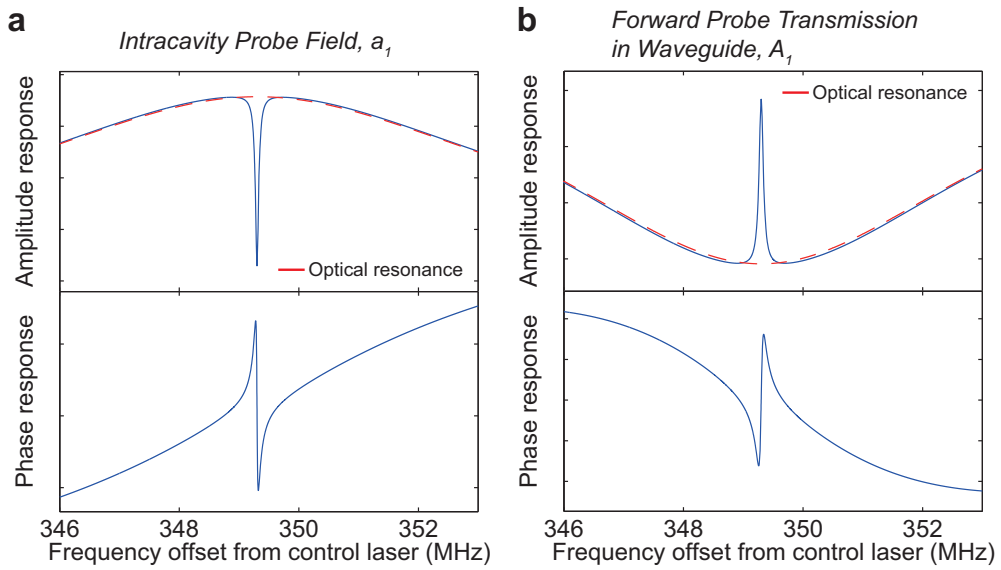

Figure 2.10: **Theoretical prediction of amplitude and phase responses for induced transparency. a.** Probe field when measured inside the cavity. **b.** Probe field transmitted and measured at the photodetector. The phase response of intracavity probe field is inverted as the light evanescently couples back to the waveguide and mix with the part of probe field that was reflected from the cavity.

Then, the following simplified system can be obtained.

$$\begin{aligned} 0 &= -\gamma_1 a_1 + f_c \\ 0 &= -\gamma_2 a_2 - i\beta u a_1 e^{i\delta t} + f_p \\ 0 &= -\gamma_B u - i\beta^* a_1^* a_2 e^{-i\delta t} \end{aligned} \tag{2.3}$$

where

$$\begin{aligned} \gamma_1 &= \kappa + i\Delta_1 \\ \gamma_2 &= \kappa + i\Delta_2 \\ \gamma_B &= \Gamma_B + i\Delta_B \end{aligned} \tag{2.4}$$

The system of equations Eq. 2.3 can then be solved to produce the steady

state amplitudes of the fields:

$$a_1 = \frac{f_c}{\gamma_1} \tag{2.5}$$

$$a_2 = \frac{f_p \gamma_B}{\gamma_2 \gamma_B + |\beta|^2 |a_1|^2} \tag{2.6}$$

$$u = \frac{-i\beta^* a_1^* a_2 e^{-i\delta t}}{\gamma_B} \tag{2.7}$$

The control laser (Eq. 2.5) excites the system, while the probe laser, described by Eq. 2.6, sweeps through the anti-Stokes optical mode of interest and experiences the induced transparency. The intracavity probe field transfer function is illustrated in Fig. 2.10a.

Note that the phase response of the probe within the cavity is in agreement with the results from previous SBS demonstrations, that is to say an anti-Stokes probe experiences a fast light response. However, the opposite result (slow light) is observed when monitoring the probe field in the waveguide ($A_2 = RF_p + iTa_2$). Here, the input probe laser field is related to input intracavity field as $F_p = -if_p/T$ [15], while R and T are the reflection and transmission coefficients at the coupler. As shown in Fig. 2.10b, a slow light behavior is observed for the probe when measured in the waveguide.

2.5.2 Induced Absorption

To understand Brillouin scattering induced absorption, the process with a Stokes probe must be considered. Here, the same set of equations used for induced transparency is employed (Eq. 2.1), except that the roles of the control and probe lasers are reversed. In other words, subscript 1 refers to the Stokes probe while subscript 2 refers to the control field. Then, the simplified system equations can be written as:

$$\begin{aligned} 0 &= -\gamma_1 a_1 - i\beta^* u^* a_2 e^{-i\delta t} + f_p \\ 0 &= -\gamma_2 a_2 + f_c \\ 0 &= -\gamma_B u - i\beta^* a_1^* a_2 e^{-i\delta t} \end{aligned} \tag{2.8}$$

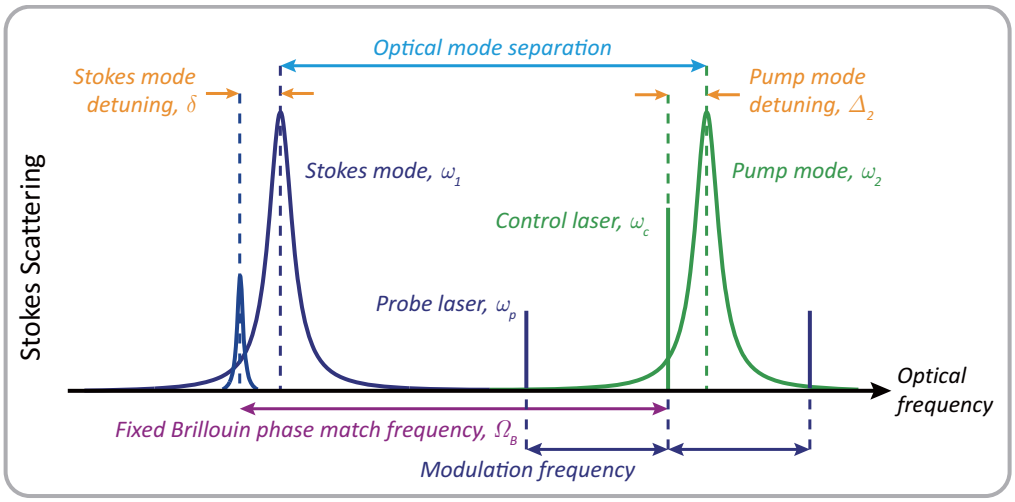

Figure 2.11: Optical frequency relationship of the coupled triplet system for absorption experiment using Stokes scattering. Opposite to anti-Stokes scattering case, the role of the pump and scattered modes is switched. Also, the probe laser sweeps in the opposite direction from higher to lower frequency.

where

$$\begin{aligned} \gamma_1 &= \kappa + i\Delta_1 \\ \gamma_2 &= \kappa + i\Delta_2 \\ \gamma_B &= \Gamma_B + i\Delta_B \end{aligned} \tag{2.9}$$

The frequency matching relationship between the fields is unchanged i.e. $\omega_2 = \omega_1 + \Omega_B$. However, as illustrated in Fig. 2.11, the detuning parameters are modified on account of the interchanged control and probe designations.

$$\begin{aligned} \Delta_1 &= \omega_1 - \omega_p \\ \Delta_2 &= \omega_2 - \omega_c \\ \Delta_B &= \Omega_B - (\omega_c - \omega_p) \end{aligned} \tag{2.10}$$

Upon solving system of equations Eq. 2.8, the intracavity probe field is described as

$$a_1 = \frac{f_p \gamma_B^*}{\gamma_1 \gamma_B^* - |\beta|^2 |a_2|^2} \tag{2.11}$$

As before, the forward probe transmission in the waveguide A_1 is described as

$$A_1 = RF_p + iTa_1 \ . \tag{2.12}$$

Again, an inversion of phase response takes place when the probe field exits the resonator and mixes with the reflected input probe that did not couple to the resonator (Fig. 2.12).

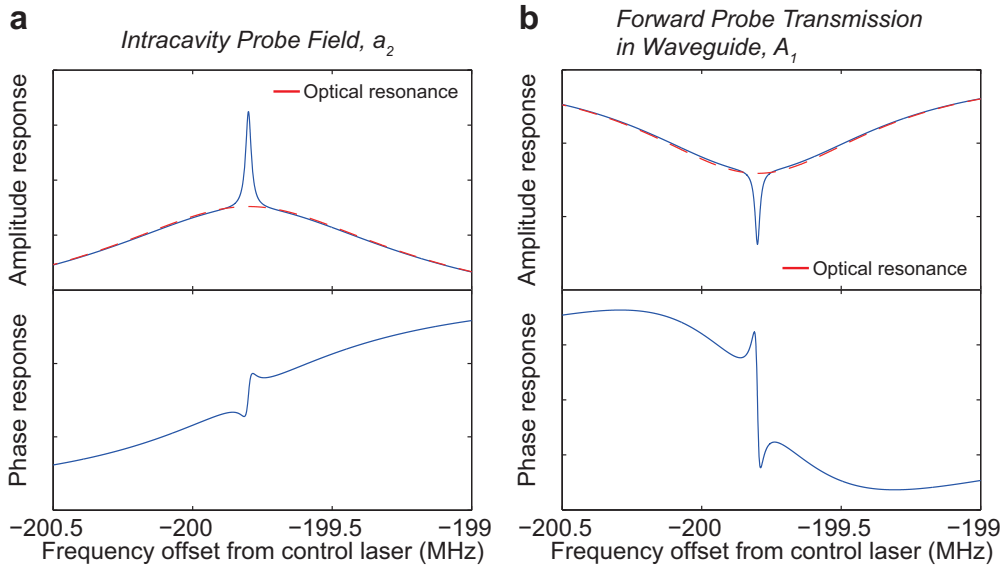

Figure 2.12: **Theoretical prediction of amplitude and phase responses for induced absorption. a.** Probe field when measured inside the cavity. **b.** Probe field transmitted and measured at the photodetector. The phase response of intracavity probe field is inverted as the light evanescently couples back to the waveguide and mix with the part of probe field that was reflected from the cavity.

2.6 Tuning Optical Mode

Although phase matching (Eq. 1.1 and 1.2) imposes strict constraints on the optical signal frequencies in the BSIT process, the transparency can be tuned by either slightly modifying the pump frequency within its optical mode, or thermally tuning the optical modes themselves (Fig. 2.13). The tuning of optical mode is also revealed from the Eq. 2.6 by modifying the detuning,

$\omega_2 - \omega_1 - \Omega_B$ (Fig. 2.14). Furthermore, the transparency depth and width can be controlled [2, 27] through the control laser power. Such frequency tunability and the ability to switch the transparency on and off are desirable in several applications [28, 29].

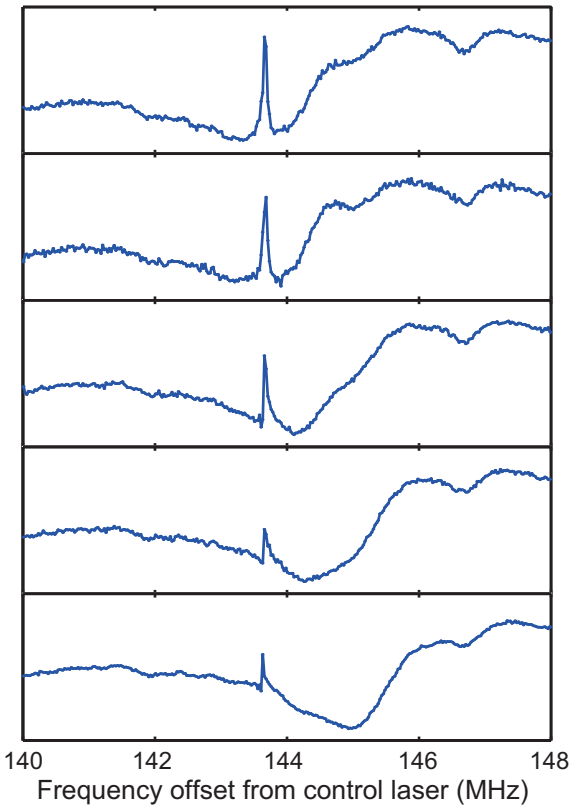

Figure 2.13: Tuning optical modes. Tuning the control laser frequency causes a relative detuning of the anti-Stokes optical mode while the transparency remains at a fixed frequency offset, Ω_B In this example, a SBS triplet with Ω_B= 143.7 MHz is used.

2.7 Strong Coupling Regime

When the coupling rate is comparable to the optical loss rate $|\beta||a_1| \approx \kappa$, the system enters the strong coupling regime [30]. In the strong coupling regime, a mode split is observed such that an optical resonance at the original frequency is completely removed. Instead, two new optical resonances which

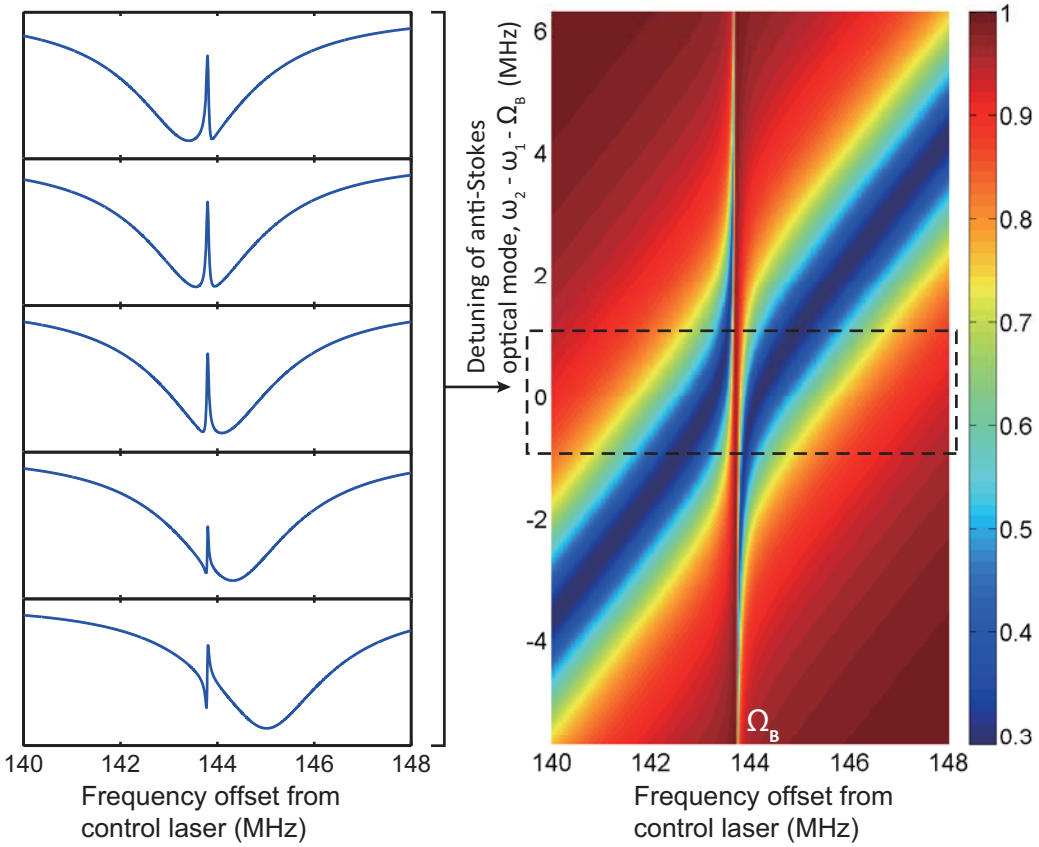

Figure 2.14: Theoretical modeling through Eq. 2.6 shows the stationary transparency at Ω_B while the anti-Stokes optical mode is tuned through the control laser frequency. This is consistent with experimental result from Fig. 2.13.

can be tuned using the coupling rate are observed.

Experimentally, the control field a_1 is used to manipulate the coupling rate. The coupling coefficient β can be held constant as it is defined by the optical modes only. In Fig. 2.15 and 2.16, the progression of the mode split with increasing control laser power is shown. Here, the strong coupling regime could be reached with only 40 μW of dropped input optical power. The optical loss rate κ=4.4 MHz and acoustic loss rate Γ_B=16.9 kHz are extracted from the experimental data.

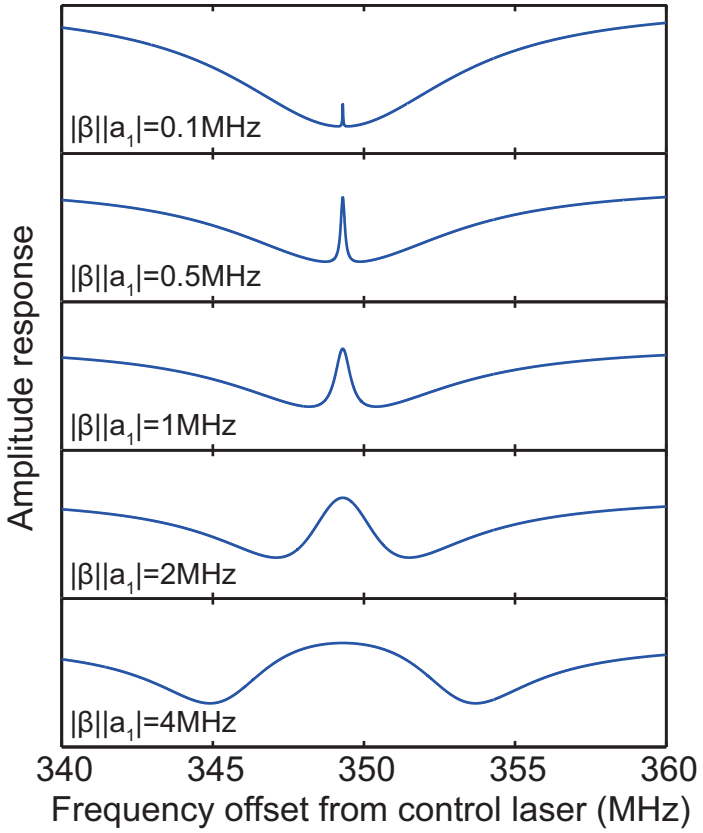

Figure 2.15: Increasing the control laser power increases the coupling rate, $|\beta||a_1|$, and the coupling rate increases the amplitude of the transparency peak. Past the strong coupling regime, the mode splitting occurs.

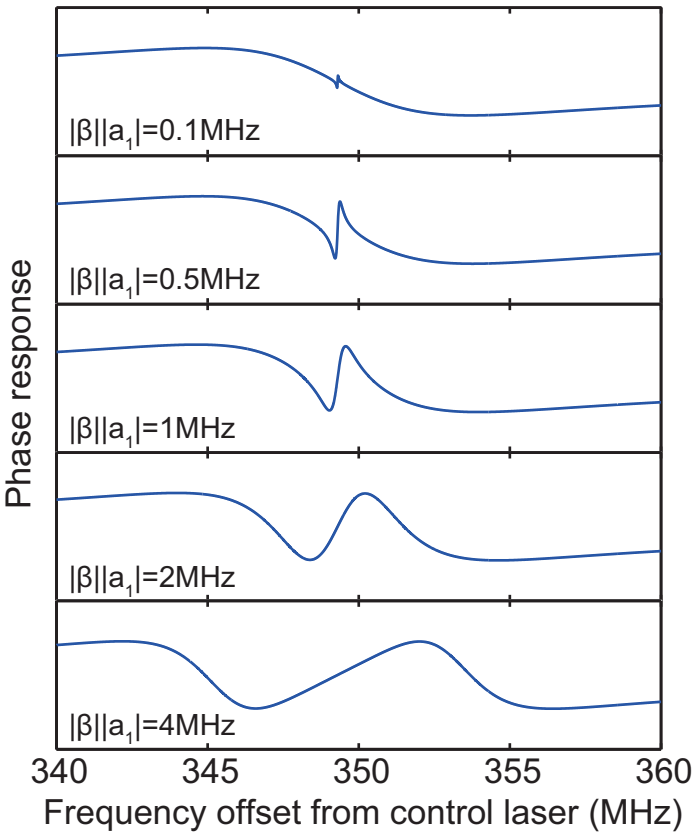

Figure 2.16: The change in phase response with increasing control laser power.

CHAPTER 3

SLOW AND FAST LIGHT

The ability to control group velocity of light is useful in several applications including optical buffering [31], optical signal processing, and optical data storage [32]. For instance, optical buffer is essential in optical fiber network as a pulse or packet of data can only be processed one at a time. Here, optical buffer is necessary to slow down a pulse in order to prevent the unwanted merging or crosstalk of the optical data. Optical signal processing and data storage are also attracting more interest as the optical transistor has been demonstrated [33] and research on optical computing is starting to emerge. In this chapter, mechanisms of delaying light pulse and how light dispersion is modified from BSIT process are explained.

3.1 Background

3.1.1 Group Velocity and Group Index

In the context of slow and fast light, it is the velocity of light "pulse" that is being modulated as oppose to the speed of light. The speed of light pulse is governed by the group index of a medium in which the light travels through. In other words, the group velocity, v_g, is determined by the group index, n_g as shown in Eq. 3.1. Therefore, the dispersion, $dn/d\omega$, must be modified to control the velocity of light pulses (Eq. 3.2).

$$v_g = \frac{c}{n_g} \tag{3.1}$$

$$n_g = n + \omega \frac{dn}{d\omega} \tag{3.2}$$

In essence, light pulse can be slowed down with positive valued dispersion

and "superluminal" speed (i.e. fast light) can be achieved with negative valued dispersion.

3.1.2 Methods of Generating of Slow and Fast Light

Resonances generate rapid changes in phase response of an optical system which can be understood as either slow or fast light depending on the sign of the phase slope (Fig. 3.1). There are many mechanisms that create such resonances. EIT and optomechanically induced transparency creates a transmission signal similar to BSIT and can be used for generating slow and fast light [9, 34]. Spectral hole burning effect through coherent parametric oscillations creates a narrow window of increased transmission, which results in slow light [35, 36]. Also, there has been demonstration of using metamaterial to engineer refractive index and generate slow light [37].

3.1.3 Kramers-Kronig Relations

Kramers-Kronig relation describes a transformation (Hilbert transform) of real to imaginary parts and vice versa of a complex function under the assumption of causality [38]. Therefore, the dispersion can be retrieved from just the transmission or absorption spectrum using the Hilbert transform. For a complex function defined as $Z(\omega) = A(\omega) + iB(\omega)$, the Hilbert transform, H, relates the real and imaginary parts in the following way.

$$\begin{aligned} A(\omega) &= H(B(\Omega)) = \frac{1}{\pi}\int_{-\infty}^{\infty}\frac{B(\Omega)}{\omega-\Omega}d\Omega \\ B(\omega) &= -H(A(\Omega)) = -\frac{1}{\pi}\int_{-\infty}^{\infty}\frac{A(\Omega)}{\omega-\Omega}d\Omega \end{aligned} \tag{3.3}$$

Based on the resonance shape from Fig. 3.1a, it is shown that a narrow resonance feature is necessary to acquire a large dispersion, $|dn/d\omega|$, and increased slow and fast light time. In case of BSIT, the linewidth of transparency peak is narrow (17 kHz) which makes BSIT an ideal system for generating slow light.

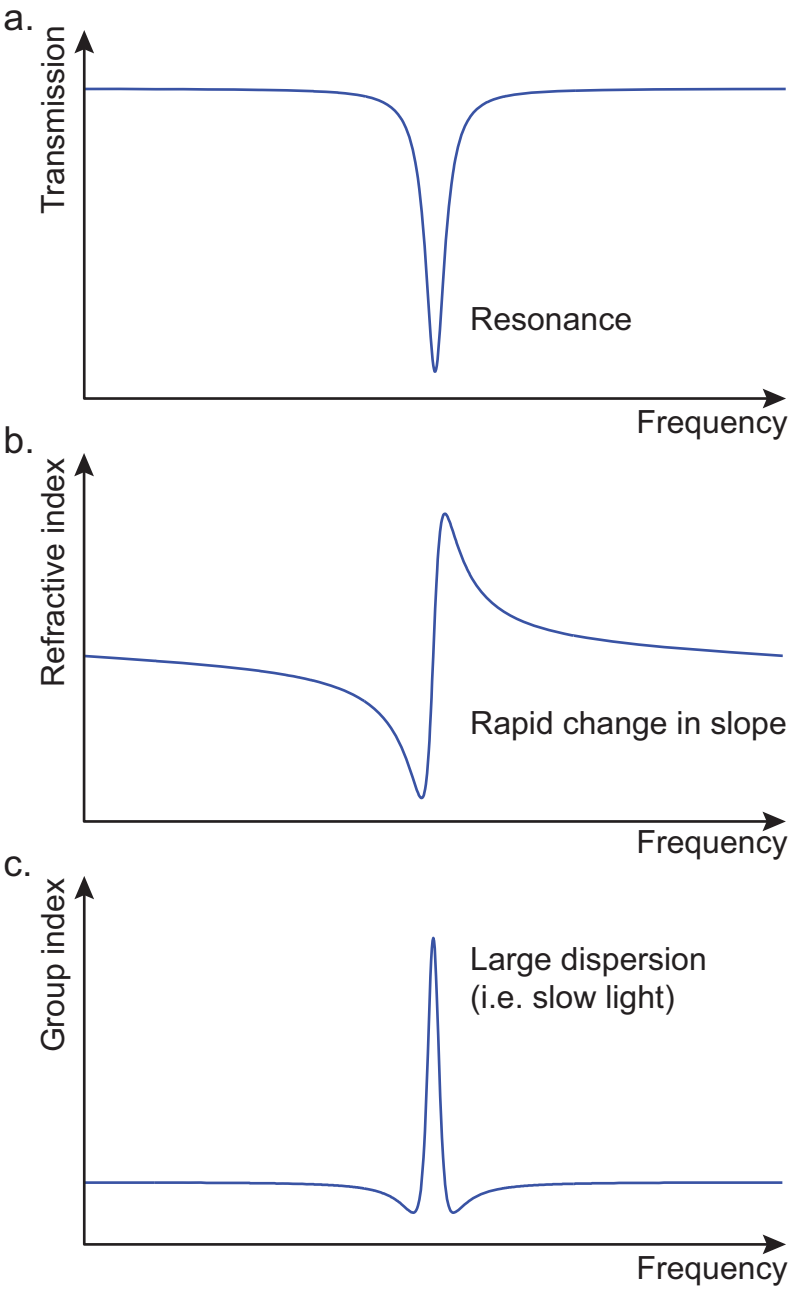

Figure 3.1: **a.** An example transmission signal with resonance dip. **b.** The refractive index calculated using the Hilbert transform of the transmission signal. **c.** The slope of the refractive index, i.e. dispersion. The positive value of group index indicates the generation of slow light.

3.2 Interpretation of Phase Response

To estimate how much group delay τ_g can be achieved (in units of seconds), we use Eq. 3.4.

$$\tau_g = \frac{d\phi}{d\omega} \tag{3.4}$$

where ϕ is phase response and ω is frequency. Using this relationship, the phase data from the induced transparency and absorption can be further analyzed.

3.2.1 Slow Light

In Eq. 3.4, positive τ_g represents an optical delay and a negative value represents an optical advancement. Therefore, the rapidly changing phase response feature with a positive slope corresponds to a very low group velocity for the optical probe i.e. "slow light"[9, 39]. The probe time delay of 110 μs is estimated from the phase response (Fig. 3.2).

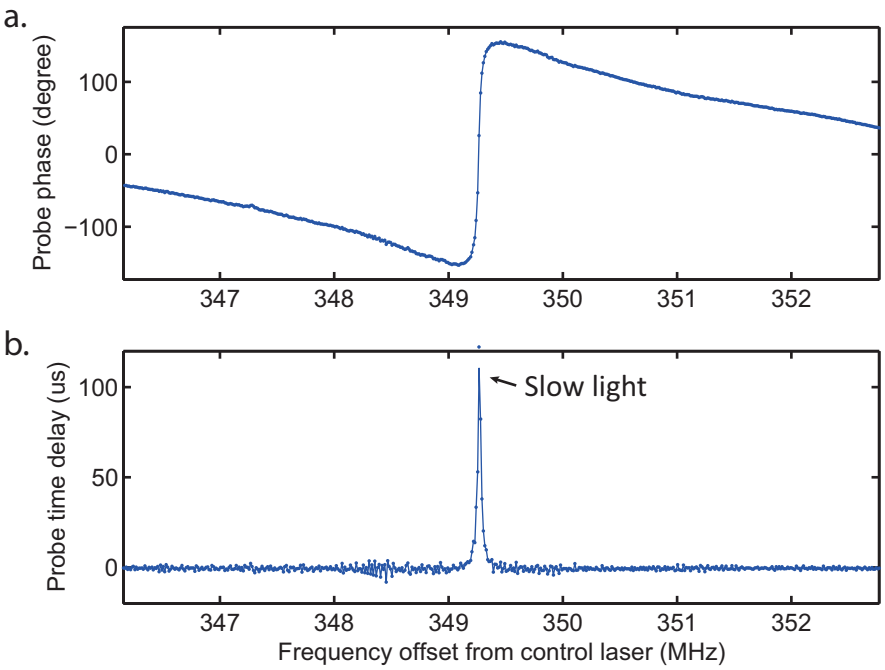

Figure 3.2: **a.** Probe phase response from induced transparency is shown. **b.** Additional probe group delay is generated compared to the transmission time without BSIT. 1 μW of laser power is used to generate time delay of 110 μs.

3.2.2 Fast Light

On the other hand, the probe phase response with a negative slope corresponds to a "fast light" dispersion feature. Based on the phase response slope, additional 35 μs fast light time advancement is estimated (Fig. 3.3).

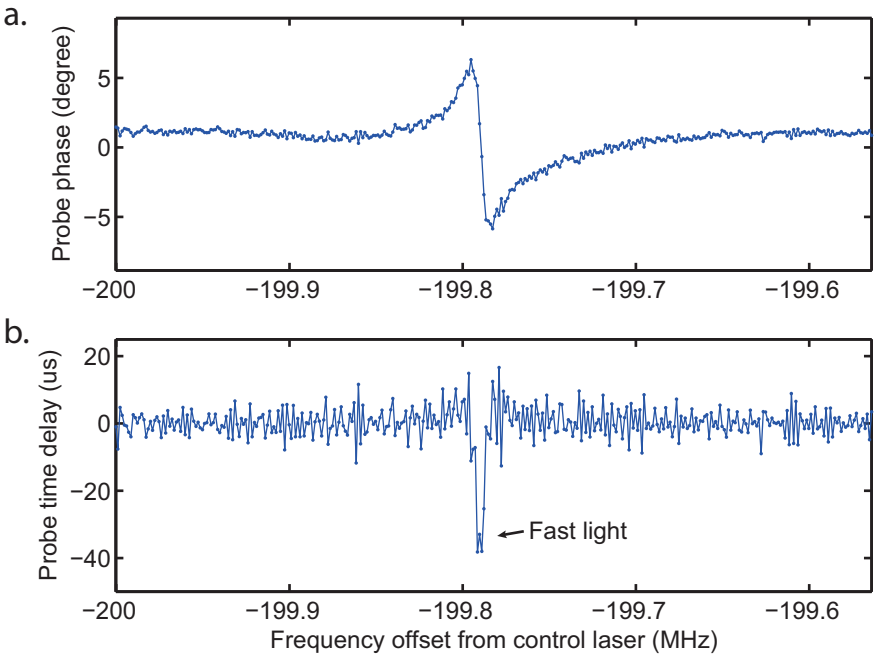

Figure 3.3: **a.** Probe phase response from induced opacity is shown. **b.** Probe time advancement is shown compared to the transmission time without Brillouin scattering induced opacity. Time advancement of 35 μs is demonstrated using 380 nW of control laser power.

3.3 Comparison of BSIT Based Slow Light with Previous Demonstrations

The typical figure of merit reported in slow and fast light systems is the product of group delay and bandwidth. However, the delay-bandwidth product in SBS systems can be arbitrarily increased within technical limits by increasing the control laser power and waveguide length [40, 41, 42, 43]. It is noted that both laser power and device size are engineering-related constraints that must be budgeted wisely. This is critically important in on-chip devices where the laser power budgets are extremely small and kilometer-long waveguides (as in fiber SBS systems) are simply impractical.

Thus, in order to make a fair comparison between different SBS based systems, a figure of merit that normalizes the effects of control laser power and device length is suggested as follows.

$$FoM = \frac{\tau_g \Gamma_B}{I_c L} \tag{3.5}$$

where τ_g is group delay, Γ_B is bandwidth, I_c is laser power, and L is device length. In other words, this FoM is simply a calculation of the intrinsic Brillouin gain in the system. By performing this normalization, a measure of the efficiency of the system for obtaining a certain delay-bandwidth product is found.

BSIT experimental data is compared against previous SBS slow light reports in Table 3.1. The resonator circumference is used as the device length L to compare our system against linear systems. It is shown that BSIT system provides a $\tau_g \Gamma_B$ product that is comparable to all previous demonstrations (order-of-magnitude is 1). In terms of the new FoM, however, our system provides a $\tau_g \Gamma_B$ product with 5 orders-of-magnitude lower power $\times$ length product than the next nearest system. This enormous engineering advantage makes our system particularly well-suited for on-chip SBS slow light systems.

Table 3.1: This table compares the figures-of-merit for various SBS slow light systems. For each publication, only the results with highest figure of merit value reported are presented. Our system has delay × bandwidth product ($\tau_g\Gamma_B$) that is on par with other SBS slow light systems. However, the power- and size- normalized figure of merit (Eq. 3.5) shows that our system is 5 orders-of-magnitude more efficient, i.e. can provide comparable $\tau_g\Gamma_B$ with 10^5 times lower power and size when compared against the next nearest prior result.

Author	Highest group delay, τ_g (μs)	Bandwidth, Γ_B (MHz)	Control laser power, I_c (mW)	Device length, L (km)	Delay × Bandwidth product, $\tau_g\Gamma_B$ (μs-MHz)	Normalized FoM, $\frac{\tau_g\Gamma_B}{I_cL}$ ($W^{-1}m^{-1}$)
This work (Slow light)	110	0.018	1	4.7×10^{-7}	1.87	3.98×10^{6}
This work (Fast light)	35	0.017	0.38	4.7×10^{-7}	0.63	3.53×10^{6}
R. Pant [44]	0.023	40	300	7×10^{-5}	0.92	4.38×10^{1}
K. Y. Song [40]	0.018	13.33	0.012	6.7×10^{0}	0.24	2.99
D. Deng [45]	0.37	1	1000	1×10^{-2}	0.37	3.69×10^{-2}
H. Ju [46]	0.04	11.24	20	2×10^{0}	0.45	1.12×10^{-2}
Y. Okawachi [41]	0.02	66.67	250	5×10^{-1}	0.4	1.07×10^{-2}
Y. Ding [27]	0.024	50	16	5×10^{1}	1.2	1.5×10^{-3}
L. Yi [43]	0.0008	812.5	100	1.25×10^{1}	0.65	5.2×10^{-4}

CHAPTER 4

PROPOSAL FOR BRILLOUIN SCATTERING OPTICAL ISOLATOR

An optical isolator is a device that allows light to propagate in only one direction. In many cases, the backscattered or reflected light can create noise or instability, or cause damage to the optical components such as a laser. All optical isolators currently available utilize the Faraday rotator media, which rotates the polarization of light in a non-reciprocal manner [47]. The challenge of using Faraday effect based optical isolator arises in applications where magnetic fields are to be avoided. Therefore, a new optical isolator design is proposed in this chapter.

4.1 Background on Faraday Optical Isolator

The optical isolator is a directional filter that blocks light based on the propagation direction. Since there is no difference in characteristic of light traveling in the opposite direction, the polarization of light is modified based on the propagation direction first using the principle of Faraday effect. The Faraday effect describes a dielectric material's tendency to rotates the light polarization non-reciprocally given a magnetic field across the medium. In other words, two light fields traveling across the Faraday rotator in an opposite direction experience the rotation in the same direction. Therefore, if light field travels across the Faraday rotator and reflects or scatters back to its original location, the polarization will not be identical to the initial polarization. By using two birefringent media or polarization filters before and after the Faraday rotator to refract and separate light with different polarization, the light may be allowed to travel only in one direction (Fig. 4.1).

Faraday rotator requires a biasing magnetic field to generate such an optical behavior. Therefore, an optical isolator typically houses a strong magnet. This is acceptable in many applications, but a magnet is difficult to integrate

onto an optical circuit as magnet has to be bonded onto the device [48]. Therefore, a non-magnetic isolator is desirable for on-chip implementation and other applications that limits the use of magnet or magnetic field within a system.

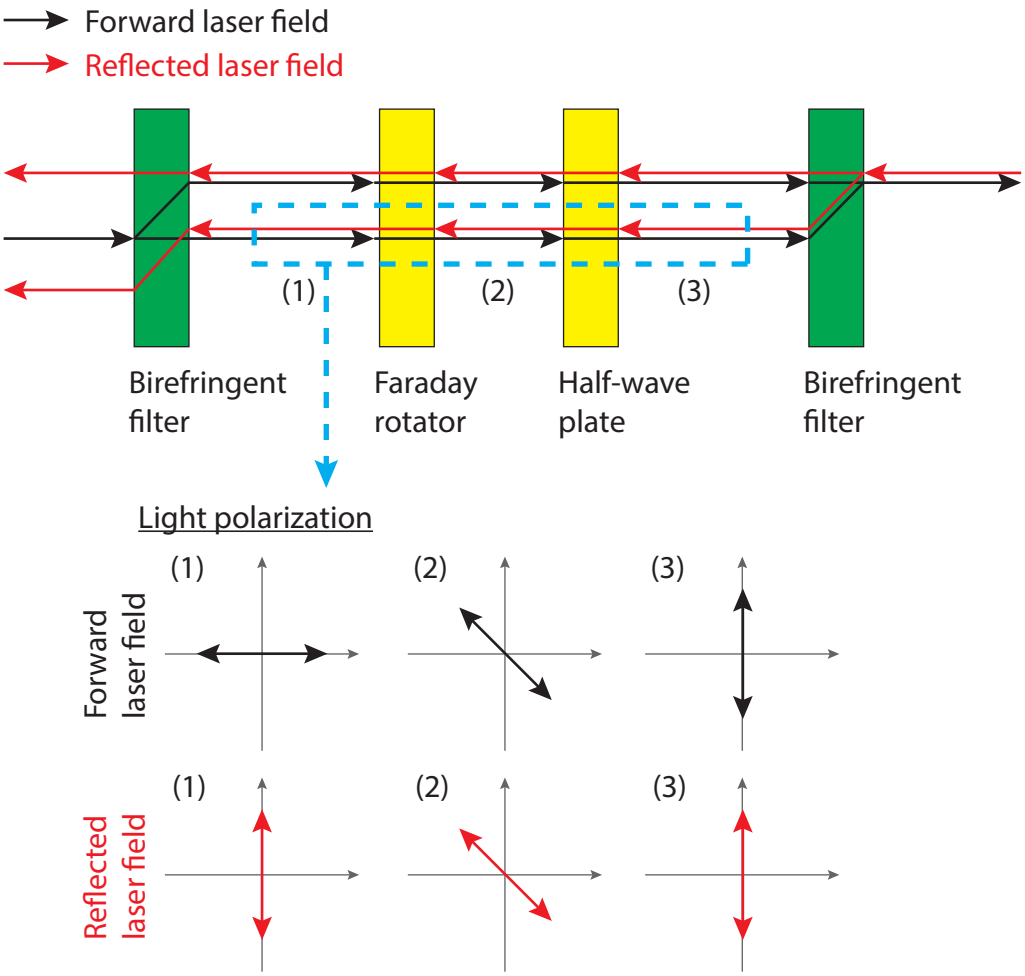

Figure 4.1: Light path and light polarization changes within an optical isolator. (Top) The reflected laser field does not travel back to the initial position of the forward propagating laser field. (Bottom) Unlike the half-wave plate, which rotates the polarization of light symmetrically, the Faraday rotator rotates the polarization non-reciprocally depending on the direction of light propagation.

4.2 Non-reciprocity in Brillouin Scattering

Brillouin scattering is non-reciprocal system due to the uni-directional nature of the traveling surface acoustic wave employed. In the omega-k diagram, the scattering pathway is supported by the optical mode in the forward direction. However, there is no optical mode separated by the acoustic parameters in both anti-Stokes and Stokes scattering frequencies in the backward direction (Fig. 4.2). This break in symmetry creates a non-reciprocity which is used for optical isolation.

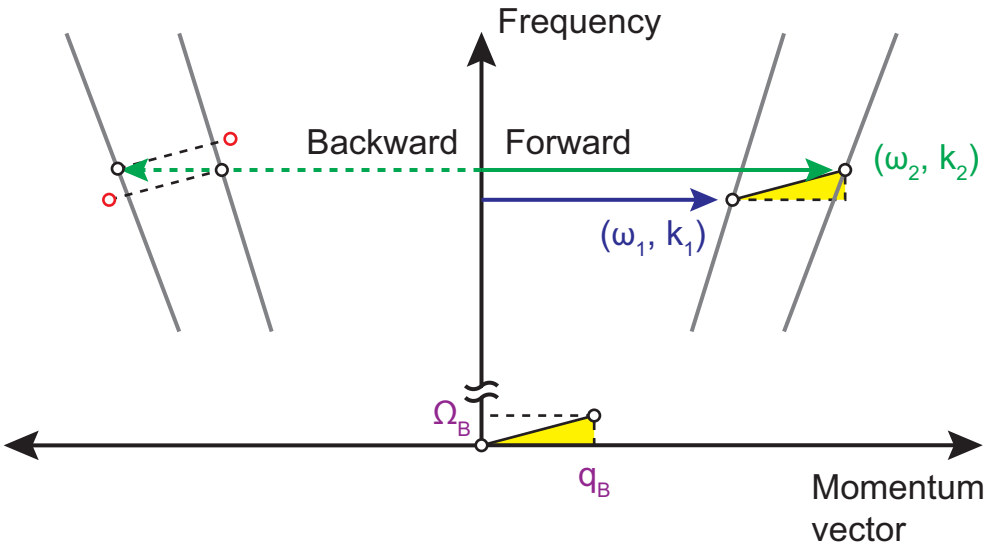

Figure 4.2: Omega-k diagram showing phase matching for forward and backward propagating optical field. (ω_1, k_1) and (ω_2, k_2) optical modes are separated by the acoustic parameters (Ω_B, q_B) in the forward direction only.

4.3 Experimental Procedure

The proposed experimental setup for demonstration of optical isolation is shown in Fig. 4.3. Once the Brillouin phase matched optical and acoustic modes are identified and induced transparency is demonstrated in the forward direction (Fig. 4.4), a second EOM is used to probe the resonator from the backward direction (Fig. 4.5). In order to prevent from actuating the acoustic mode in the backward direction, the bias voltage for the second EOM is

adjusted to minimize the control or pump signal propagating in the backward direction at the control laser frequency.

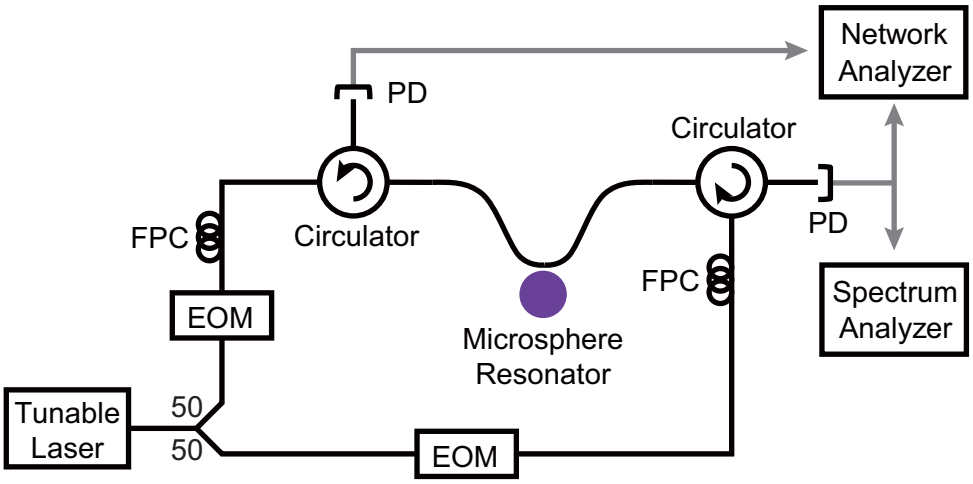

Figure 4.3: Experimental setup for demonstration of optical isolator. In addition to the experimental setup for BSIT (Fig. 2.4), circulators and an EOM are used to probe the device from both forward and backward direction.

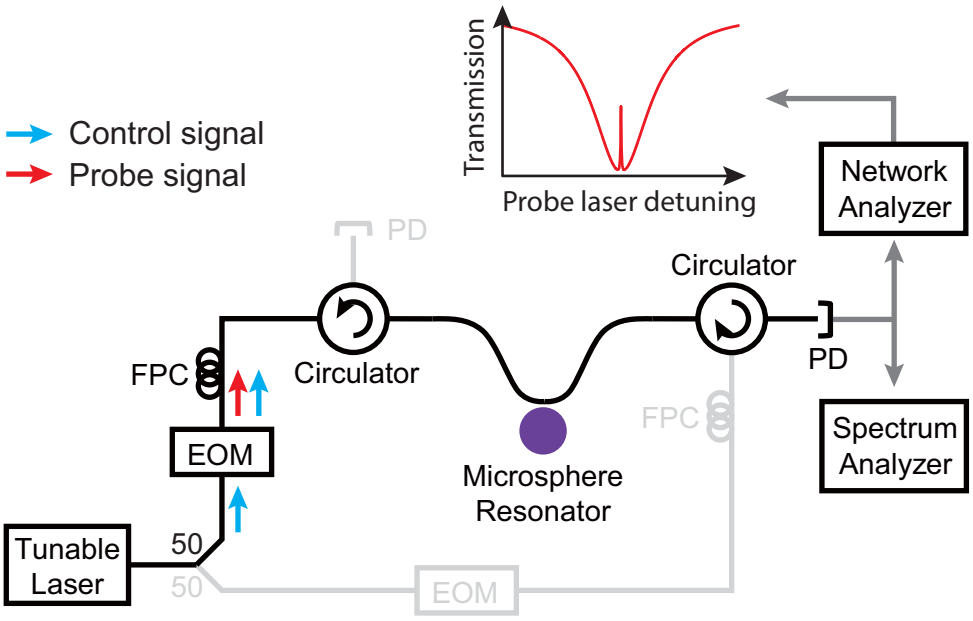

Figure 4.4: Optical isolator experiment showing forward probing. The optical isolator is switched on using the laser signal going forward direction. This will allow the probe signal (sideband from EOM) propagation in the forward direction at the transparency region as shown in the inset.

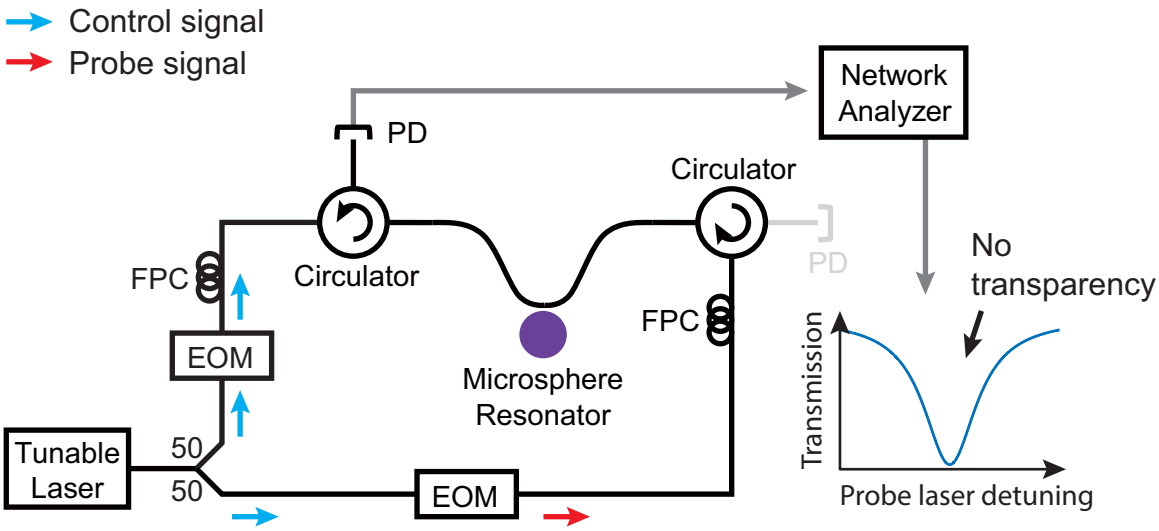

Figure 4.5: Optical isolator experiment showing backward probing. A modulation input to the EOM in the forward direction is switched off to transmit only the control signal. All of laser signal going in the backward direction is modulated to the probe signal to prevent induced transparency in the backward direction. The probe signal (sideband from EOM) is expected to be resonantly absorbed into the resonator.

CHAPTER 5

INTEGRATION TO OPTICAL CIRCUIT

Here, the possibility of integration to optical circuit is discussed. As mentioned in Ch. 4, BSIT based optical isolators have an advantage of easier on-chip fabrication over other optical isolators which require magnetic fields. Also, the on-chip design is preferred in order to avoid extraneous light coupling for applications with limited laser power output.

5.1 Resonator and Waveguide Material

For the integration to optical circuit, the waveguide must be fabricated in proximity of the resonator. Therefore, the material choice with consideration for the fabrication of the resonator, waveguide and cladding is discussed here.

5.1.1 On Chip Waveguide

The microsphere resonators used in BSIT experiment are fabricated using silicon dioxide (SiO_2) due to its excellent optical transmission characteristic in C-band (1530 to 1565 nm). In this wavelength, the optical loss is typically less than 0.2 dB/km [20]. SiO_2 is commonly used material in semiconductor industry and therefore, is compatible with CMOS fabrication techniques [49]. The difficulty in using SiO_2, however, lies in fabrication of on-chip waveguide. The waveguide is typically made up of a core and a cladding which surrounds the core and confines the light within the core. The cladding is required to have the refractive index that is lower than the refractive index of the core. This allows the light to be confined within the core by the total internal reflection. However, the material with index lower than SiO_2 (1.45) is rare besides air or vacuum, which cannot support released structures.

A good alternative to SiO_2 is silicon nitride (SiN_x). SiN_x is also CMOS

fabrication compatible and is optically transparent at C-band [49, 50]. But most importantly, SiN_x has a refractive index of 1.99. Therefore, SiO_2 makes a good cladding material for SiN_x core.

5.1.2 Brillouin Gain

Brillouin gain is a material property which determines the degree of amplification from Brillouin scattering. In the context of BSIT and slow light, Brillouin gain also determines the group delay. Brillouin gain, g_o, is defined in Eq. 5.1.

$$g_o = \frac{\gamma_e^2 \omega^2}{nvc^3 \rho_o \Gamma_B} \tag{5.1}$$

where g_o is Brillouin gain, γ_e is electrostrictive coefficient, ω is laser frequency, n is refractive index, v is speed of sound, c is speed of light in vacuum, ρ_o is material density, and Γ_B is acoustic linewidth (or inverse of phonon lifetime $\tau = \Gamma_B^{-1}$) [1]. In Eq. 5.1, it is important to note that the Brillouin gain does not have inverse relationship to the refractive index, but instead the Brillouin gain is proportional to n^7 because the electrostrictive coefficient is proportional to n^4 [51].

Therefore, the material with different values of electrostrictive coefficient and refractive index may be explored. For instance, chalcogenide has a very high electrostrictive coefficient which will further enhance SBS effects [52]. And there are materials with negative electrostrictive coefficient [53] which may bring interesting applications in the future.

5.2 Fabrication of Device on Chip

5.2.1 On Chip Resonator Design

The microsphere resonator is used for demonstration of BSIT off chip. However, the fabrication of 3-dimensional structure such as a sphere is challenging especially on-chip. Therefore, alternative options are considered here. There are several resonator design that can be used for BSIT including disc [54], double disc [55], ring [56], toroid [57], racetrack [58], Bragg-reflector [59],

photonic crystal [60] and many more. Here, disc, toroid and ring resonators are chosen and fabricated (Fig. 5.1).

Among the three designs, the disc resonator etched using hydrogen fluoride (Fig. 5.1a) is the most promising for integration to optical circuit. This wedged disc resonator design is shown to provide good optical mode confinement as well as high quality factor [54]. On the other hand, the ring resonator etched using RIE etcher has low quality factor due to the surface roughness caused from the switching process (Fig. 5.1c, d). Lastly, the toroid resonator lased using CO_2 laser showed good device performance (Fig. 5.1b). However, the lasing process is challenging when implemented with a waveguide in proximity of the resonator.

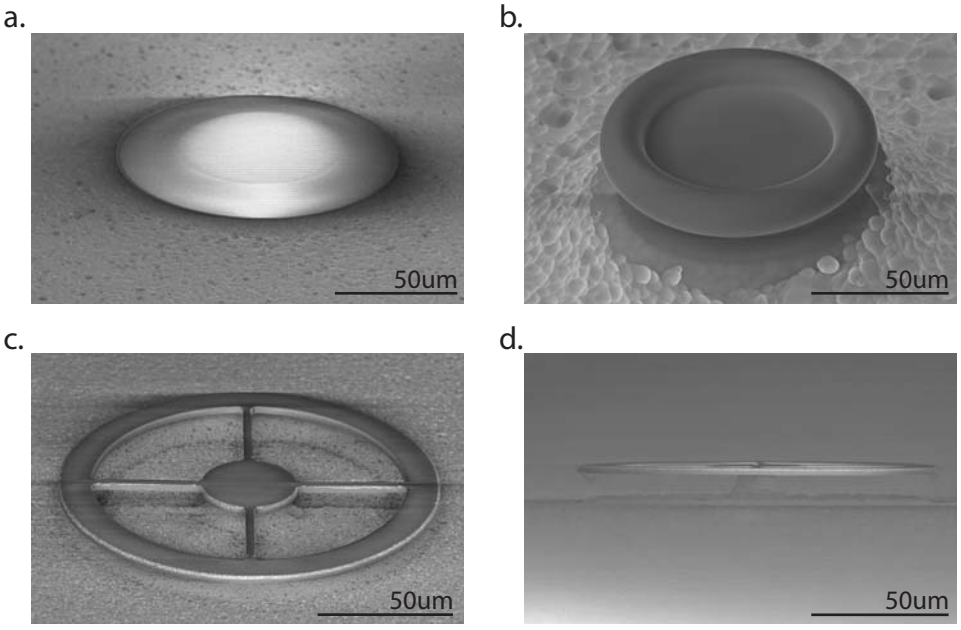

Figure 5.1: **Scanning electron microscope (SEM) images of resonators. a.** Disc resonator etched using HF. Wedge is created on the top side. **b.** Toroid resonator formed by heating disc resonator with CO_2 laser. **c.** Ring resonator etched using RIE. **d.** Side view of the ring resonator.

5.2.2 Fabrication Procedure

The fabrication procedure is outlined in Fig. 5.2. A silicon wafer with up to 10 μm of SiO_2 grown on top is commercially available from WRS Materials. Other resonator materials such as SiN_x, gallium nitride, and many others may

be used instead of SiO_2. For the fabrication of the resonators from Fig. 5.1, silicon wafer with 2.5 μm of thermally grown SiO_2 is used. With the substrate prepared, the resonator design is patterned on the photoresist using either conventional photolithography or electron beam lithography for smaller, sub micron features. The SiO_2 layer is etched using reactive ion etching (RIE) or chemically using hydrogen fluoride (HF). SiN_x can be etched using RIE or chemically using hot phosphoric acid (H_3PO_4). RIE etched device typically has a vertical but rough sidewall. On the other hand, HF etched device has slanted but relatively smooth sidewall. To release the resonator from the silicon substrate, xenon difluoride (XeF_2) etching is used. XeF_2 aggressively etches the silicon but stays relatively inert to dielectrics such as SiO_2 and SiN_x (selectivity to silicon of 1:1000 or higher) [49]. This releasing or undercut prevents the light from escaping the resonator as it forms a low index air cladding.

After the disc resonator is fabricated, it can be heated by CO_2 laser to form a toroid resonator (Fig. 5.3). Although it is more difficult to place a waveguide in proximity, the toroid resonator can provide higher quality factor as the surface roughness is removed by lasing and light is better confined within the resonator [54, 57].

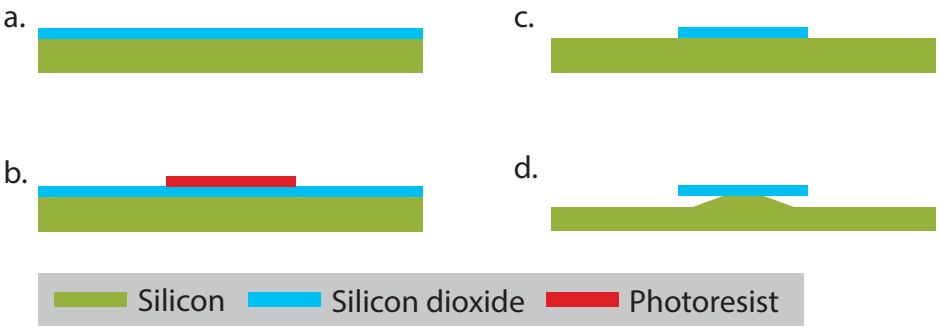

Figure 5.2: **Outline of on-chip resonator fabrication procedure. a.** Silicon wafer with SiO_2 film is purchased. Oxide can also be thermally grown on silicon wafer. **b.** Photoresist is spun on, patterned and developed. **c.** SiO_2 is etched using RIE or HF. **d.** Undercut is made by etching silicon using XeF_2 etcher.

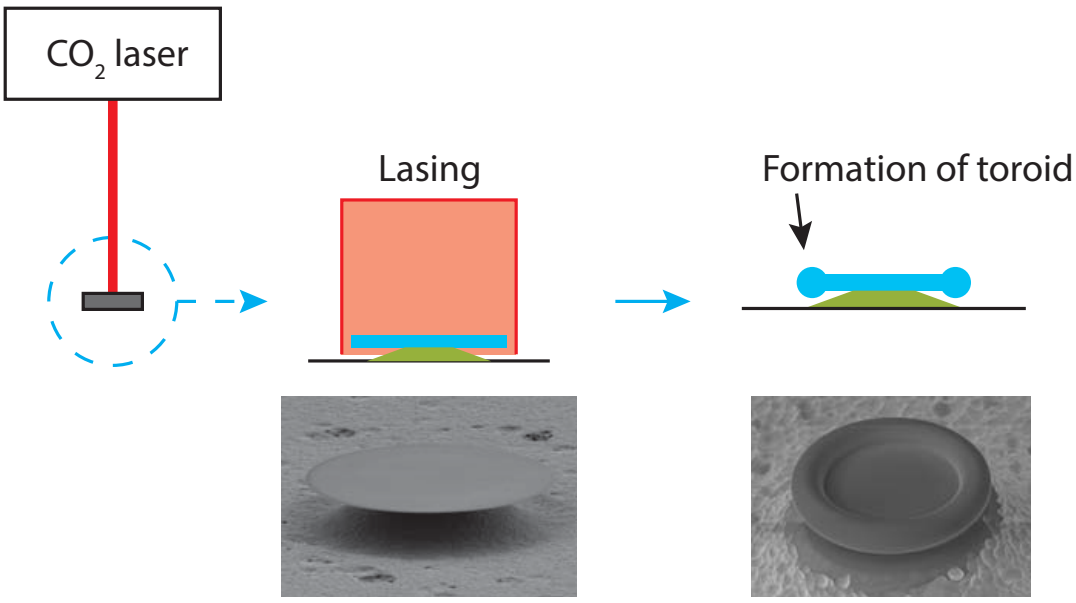

Figure 5.3: Fabrication of toroid resonator. The CO_2 laser provides the heat from the top side of the disc resonator. The laser is focused such that the beam diameter is slightly larger than the diameter of the resonator. As the suspended region of the disc resonator melts, the material reflows and forms a toroid. In the process, the silicon substrate acts as a heat sink to prevent damage to the resonator.

CHAPTER 6

CONCLUSION

In this work, induced transparency is demonstrated using SBS acousto-optic interaction phase matched with a long-lived high-coherence phonon mode. Brillouin scattering induced transparency (BSIT) enables slow and fast light generation with five-orders of magnitude higher delay-bandwidth product than state-of-the-art SBS systems of a chosen power and size budget.

There are several ways in which this work should be further pursued. First, the operating laser wavelength may be expanded. This experiment was carried out using a C-band laser (1530 to 1565 nm). However, the Brillouin scattering process is not limited to C-band nor infrared wavelength range. As there are optical applications that require operating wavelength of different wavelengths, further investigation of BSIT and optical isolation at different wavelength is planned.

Further, the operating bandwidth of the slow light and optical isolation is to be increased. The achieved bandwidth of 17 kHz has limited applications due to its inability to effectively process short pulses. To resolve this issue, several solutions are considered. Poulton et. al. demonstrated increased bandwidth in Brillouin scattering based frequency comb by engineering the dispersion line of the two optical fields to match in parallel, which theoretically allows the Brillouin phase matching to occur for all optical frequencies [29]. Also, frequency dithering of the control laser is known for increasing the bandwidth [61]. Frequency dithered input signal can excite more than one acoustic mode at slightly different frequencies. In effect, the operating bandwidth will be increased.

Lastly, the slow and fast light and optical isolation experiment has to be carried out. The slow and fast light time is calculated based on the phase response of a probing optical signal. The experiment in which a pulse is sent and measured to show exactly how much delay can be achieved will give a concrete proof of the BSIT slow light system. Also, the optical isolation

experiment where the light is allowed to propagate only in one direction should be carried out. Although the non-reciprocity in Brillouin scattering system is well-known [62, 63], an experiment where the probe is sent from both forward and backward direction should be performed to prove the non-reciprocity.

REFERENCES

[1] R. W. Boyd, *Nonlinear Optics*, 3rd ed. Elsevier, 2008, Chapter 9.

[2] G. Bahl, M. Tomes, F. Marquardt, and T. Carmon, "Observation of spontaneous brillouin cooling," *Nat Phys*, vol. 8, no. 3, pp. 203–207, Mar. 2012.

[3] K. O. Hill, B. S. Kawasaki, and D. C. Johnson, "cw brillouin laser," *Applied Physics Letters*, vol. 28, no. 10, pp. 608–609, 1976.

[4] K.-J. Boller, A. Imamolu, and S. E. Harris, "Observation of electromagnetically induced transparency," *Phys. Rev. Lett.*, vol. 66, pp. 2593–2596, May 1991.

[5] S. Zhang, D. A. Genov, Y. Wang, M. Liu, and X. Zhang, "Plasmon-induced transparency in metamaterials," *Phys. Rev. Lett.*, vol. 101, p. 047401, Jul 2008.

[6] N. Liu, L. Langguth, T. Weiss, J. Kästel, M. Fleischhauer, T. Pfau, and H. Giessen, "Plasmonic analogue of electromagneticallyinduced transparency at the Drude damping limit," *Nature Materials*, vol. 8, no. 9, pp. 758–762, July 2009.

[7] D. Smith, H. Chang, K. Fuller, A. Rosenberger, and R. Boyd, "Coupled-resonator-induced transparency," *Physical Review A*, vol. 69, no. 6, p. 063804, June 2004.

[8] S. Weis, R. Rivière, S. Deléglise, E. Gavartin, O. Arcizet, A. Schliesser, and T. J. Kippenberg, "Optomechanically induced transparency." *Science*, vol. 330, no. 6010, pp. 1520–1523, Dec. 2010.

[9] A. H. Safavi-Naeini, T. P. M. Alegre, J. Chan, M. Eichenfield, M. Winger, Q. Lin, J. T. Hill, D. E. Chang, and O. Painter, "Electromagnetically induced transparency and slow light with optomechanics," *Nature*, vol. 472, no. 7341, pp. 69–73, Apr. 2011.

[10] L. V. Hau, S. E. Harris, Z. Dutton, and C. H. Behroozi, "Light speed reduction to 17 metres per second in an ultracold atomic gas," *Nature*, vol. 397, no. 6720, pp. 594–598, 1999.

[11] C. Dong, V. Fiore, M. C. Kuzyk, and H. Wang, "Transient optomechanically induced transparency in a silica microsphere," *Physical Review A*, vol. 87, p. 055802, May 2013.

[12] G. Bahl, J. Zehnpfennig, M. Tomes, and T. Carmon, "Stimulated optomechanical excitation of surface acoustic waves in a microdevice," *Nat Commun*, vol. 2, pp. 403–, July 2011.

[13] I. S. Grudinin, A. B. Matsko, and L. Maleki, "Brillouin lasing with a CaF_2 whispering gallery mode resonator," *Phys. Rev. Lett.*, vol. 102, no. 4, p. 043902, Jan 2009.

[14] M. Tomes and T. Carmon, "Photonic micro-electromechanical systems vibrating at X-band (11-GHz) rates," *Phys. Rev. Lett.*, vol. 102, no. 11, p. 113601, March 2009.

[15] M. Gorodetsky and V. S. Ilchenko, "Optical microsphere resonators: optimal coupling to high-Q whispering-gallery modes," *Journal of the Optical Society of America B*, vol. 16, no. 1, pp. 147–154, 1999.

[16] R. W. Boyd and D. J. Gauthier, "Controlling the velocity of light pulses," *Science*, vol. 326, no. 5956, pp. 1074–1077, 2009.

[17] J. C. Knight, G. Cheung, F. Jacques, and T. A. Birks, "Phase-matched excitation of whispering-gallery-mode resonances by a fiber taper," *Opt Lett*, vol. 22, pp. 1129–1131, 1997.

[18] H. Onodera, I. Awai, and J. ichi Ikenoue, "Refractive-index measurement of bulk materials: prism coupling method," *Appl. Opt.*, vol. 22, no. 8, pp. 1194–1197, Apr 1983.

[19] H. Li, Z. Cao, H. Lu, and Q. Shen, "Free-space coupling of a light beam into a symmetrical metal-cladding optical waveguide," *Applied Physics Letters*, vol. 83, no. 14, pp. 2757–2759, 2003.

[20] "Corning optical fiber SMF-28e+," http://www.corning.com/opticalfiber/index.aspx, accessed: 2014-07-19.

[21] "Fusion splice ericsson FSU 975," http://ericsson.fiberoptic.com/fsu-975.htm, accessed: 2014-07-19.

[22] "Newport 125 MHz & 1 GHz Photoreceivers," http://www.newport.com/125-MHz-and-1-GHz-Photoreceivers/917956/1033/info.aspx, accessed: 2014-07-19.

[23] "Tektronix RSA6000 Spectrum Analyzer," http://www.tek.com/spectrum-analyzer/rsa6000, accessed: 2014-07-19.

[24] "Agilent 4395A Network/Spectrum/Impedance Analyzer," http://www.home.agilent.com/en/pd-1000000864%3Aepsg%3Apro-pn-4395A/network-spectrum-impedance-analyzer?&cc=US&lc=eng, accessed: 2014-07-19.

[25] T. J. Kippenberg, H. Rokhsari, T. Carmon, A. Scherer, and K. J. Vahala, "Analysis of radiation-pressure induced mechanical oscillation of an optical microcavity," *Phys. Rev. Lett.*, vol. 95, no. 3, p. 033901, Jul 2005.

[26] G. S. Agarwal and S. S. Jha, "Multimode phonon cooling via three-wave parametric interactions with optical fields," *Phys. Rev. A*, vol. 88, p. 013815, Jul 2013.

[27] Y. Ding, L. Chen, and S. Shen, "Slow and fast light based on SBS with the spectrum tailoring," *Optik - International Journal for Light and Electron Optics*, vol. 125, pp. 2181–2184, 2014.

[28] X. Huang and S. Fan, "Complete all-optical silica fiber isolator via stimulated brillouin scattering," *Lightwave Technology, Journal of*, vol. 29, no. 15, pp. 2267–2275, Aug 2011.

[29] C. G. Poulton, R. Pant, A. Byrnes, S. Fan, M. J. Steel, and B. J. Eggleton, "Design for broadband on-chip isolator using stimulated brillouin scattering in dispersion-engineered chalcogenide waveguides," *Opt. Express*, vol. 20, no. 19, pp. 21 235–21 246, Sep 2012.

[30] M. Fleischhauer, A. Imamoglu, and J. P. Marangos, "Electromagnetically induced transparency: Optics in coherent media," *Rev. Mod. Phys.*, vol. 77, pp. 633–673, Jul 2005.

[31] R. W. Boyd, D. J. Gauthier, and A. L. Gaeta, "Applications of slow light in telecommunications," *Opt. Photon. News*, vol. 17, no. 4, pp. 18–23, Apr 2006.

[32] E. Parra and J. R. Lowell, "Toward applications of slow light technology," *Opt. Photon. News*, vol. 18, no. 11, pp. 40–45, Nov 2007.

[33] W. Chen, K. M. Beck, R. Bucker, M. Gullans, M. D. Lukin, H. Tanji-Suzuki, and V. Vuletic, "All-optical switch and transistor gated by one stored photon," *Science*, vol. 341, no. 6147, pp. 768–770, 2013.

[34] M. D. Lukin and A. Imamoglu, "Controlling photons using electromagnetically induced transparency," *Nature*, vol. 413, no. 6853, pp. 273–276, Sep. 2001.

[35] A. V. Turukhin, V. S. Sudarshanam, M. S. Shahriar, J. A. Musser, B. S. Ham, and P. R. Hemmer, "Observation of ultraslow and stored light pulses in a solid," *Phys. Rev. Lett.*, vol. 88, p. 023602, Dec 2001.

[36] M. S. Bigelow, N. N. Lepeshkin, and R. W. Boyd, "Observation of ultraslow light propagation in a ruby crystal at room temperature," *Phys. Rev. Lett.*, vol. 90, p. 113903, Mar 2003.

[37] K. L. Tsakmakidis, A. D. Boardman, and O. Hess, "/'trapped rainbow/' storage of light in metamaterials," *Nature*, vol. 450, no. 7168, pp. 397–401, Nov. 2007.

[38] R. D. L. KRONIG, "On the theory of dispersion of x-rays," *J. Opt. Soc. Am.*, vol. 12, no. 6, pp. 547–556, Jun 1926.

[39] R. W. Boyd and D. J. Gauthier, ""Slow" and "fast" light," *Progress in Optics*, vol. 43, pp. 497–530, 2002.

[40] K. Y. Song, M. G. Herráez, and L. Thévenaz, "Observation of pulse delaying and advancement in optical fibers using stimulated Brillouin scattering," *Opt. Express*, vol. 13, no. 1, pp. 82–88, 2005.

[41] Y. Okawachi, M. Bigelow, J. Sharping, Z. Zhu, A. Schweinsberg, D. Gauthier, R. Boyd, and A. Gaeta, "Tunable All-Optical Delays via Brillouin Slow Light in an Optical Fiber," *Physical Review Letters*, vol. 94, no. 15, p. 153902, Apr. 2005.

[42] L. Thévenaz, "Slow and fast light in optical fibres," *Nature Photonics*, vol. 2, no. 8, pp. 474–481, 2008.

[43] L. Yi, L. Zhan, W. Hu, and Y. Xia, "Delay of broadband signals using slow light in stimulated brillouin scattering with phase-modulated pump," *Photonics Technology Letters, IEEE*, vol. 19, no. 8, pp. 619–621, April 2007.

[44] R. Pant, A. Byrnes, C. G. Poulton, E. Li, D.-Y. Choi, S. Madden, B. Luther-Davies, and B. J. Eggleton, "Photonic-chip-based tunable slow and fast light via stimulated brillouin scattering," *Opt. Lett.*, vol. 37, no. 5, pp. 969–971, Mar 2012.

[45] D. Deng, W. Gao, M. Liao, Z. Duan, T. Cheng, T. Suzuki, and Y. Ohishi, "Superluminal propagation in a highly nonlinear fiber embedded in a brillouin laser ring cavity," *Proc. SPIE*, vol. 8982, p. 89821J, 2014.

[46] H. Ju, L. Ren, X. Lin, J. Liang, and C. Ma, "Wide-range continuously-tunable slow-light delay line based on stimulated brillouin scattering," *Photonics Technology Letters, IEEE*, vol. 25, no. 19, pp. 1920–1923, Oct 2013.

[47] L. J. Aplet and J. W. Carson, "A faraday effect optical isolator," *Appl. Opt.*, vol. 3, no. 4, pp. 544–545, Apr 1964.

[48] Y. Shoji, M. Ito, Y. Shirato, and T. Mizumoto, "Mzi optical isolator with si-wire waveguides by surface-activated direct bonding," *Opt. Express*, vol. 20, no. 16, pp. 18 440–18 448, Jul 2012.

[49] K. Williams and R. Muller, "Etch rates for micromachining processing," *Microelectromechanical Systems, Journal of*, vol. 5, no. 4, pp. 256–269, Dec 1996.

[50] H. R. Philipp, "Optical properties of silicon nitride," *Journal of The Electrochemical Society*, vol. 120, no. 2, pp. 295–300, 1973.

[51] W. Qiu, P. T. Rakich, H. Shin, H. Dong, M. Soljačić, and Z. Wang, "Stimulated brillouin scattering in nanoscale silicon step-index waveguides: a general framework of selection rules and calculating sbs gain," *Opt. Express*, vol. 21, no. 25, pp. 31 402–31 419, Dec 2013.

[52] R. Pant, C. G. Poulton, D.-Y. Choi, H. Mcfarlane, S. Hile, E. Li, L. Thévenaz, B. Luther-Davies, S. J. Madden, and B. J. Eggleton, "On-chip stimulated Brillouin scattering," *Optics Express*, vol. 19, no. 9, pp. 8285–8290, 2011.

[53] A. Turik, A. Yesis, and L. Reznitchenko, "Negative longitudinal electrostriction in polycrystalline ferroelectrics: a nonlinear approach," *Journal of Physics: Condensed Matter*, vol. 18, no. 20, p. 4839, 2006.

[54] H. Lee, T. Chen, J. Li, K. Y. Yang, S. Jeon, O. Painter, and K. J. Vahala, "Chemically etched ultrahigh-q wedge-resonator on a silicon chip," *Nat Photon*, vol. 6, no. 6, pp. 369–373, June 2012.

[55] C. G. K. H. Nygaard and T. A. Fjeldly, "Stacked coupled-disk mems rresonator for rf applications," in *Technical Proceedings of the 2008 NSTI Nanotechnology Conference and Trade Show*, vol. 3, 2008, pp. 478–480.

[56] S. Tallur and S. A. Bhave, "Simultaneous radiation pressure induced heating and cooling of an opto-mechanical resonator," *Applied Physics Letters*, vol. 100, no. 11, pp. –, 2012.

[57] D. Armani, T. Kippenberg, S. Spillane, and K. Vahala, "Ultra-high-Q toroid microcavity on a chip," *Nature*, vol. 421, no. 6926, pp. 925–928, Feb 2003, 10.1038/nature01371.

[58] V. T. K. Sauer, Z. Diao, M. R. Freeman, and W. K. Hiebert, "Optical racetrack resonator transduction of nanomechanical cantilevers," *Nanotechnology*, vol. 25, no. 5, pp. 055 202–, 2014.

[59] J.-M. Le Floch, M. Tobar, D. Cros, and J. Krupka, "High q-factor distributed bragg reflector resonators with reflectors of arbitrary thickness," *Ultrasonics, Ferroelectrics and Frequency Control, IEEE Transactions on*, vol. 54, no. 12, pp. 2689–2695, December 2007.

[60] H. Altug and J. Vuckovic, "Two-dimensional coupled photonic crystal resonator arrays," in *Conference on Lasers and Electro-Optics/International Quantum Electronics Conference and Photonic Applications Systems Technologies*. Optical Society of America, 2004. http://www.opticsinfobase.org/abstract.cfm?URI=IQEC-2004-IThI2 p. IThI2.

[61] M. G. Herráez, K. Y. Song, and L. Thévenaz, "Arbitrary-bandwidth brillouin slow light in optical fibers," *Opt. Express*, vol. 14, no. 4, pp. 1395–1400, Feb 2006.

[62] M. S. Kang, A. Butsch, and P. S. J. Russell, "Reconfigurable light-driven opto-acoustic isolators in photonic crystal fibre," *Nat Photon*, vol. 5, no. 9, pp. 549–553, Sep. 2011.

[63] M. G. Zhanuzakov, A. A. Zozulya, and V. T. Tikhonchuk, "Nonlinear theory of a self-reversing ring stimulated brillouin scattering mirror," *Soviet Journal of Quantum Electronics*, vol. 19, no. 2, p. 254, 1989.